metals

MDPI

Article

Depth-Resolved Surface Integrity Evolution and Hydrodynamic Erosion Mechanisms in Abrasive Water Jet Machining of Dissimilar Stainless Steel–Carbon Steel Welds

Mohammad S. Alsoufi

Department of Mechanical Engineering, College of Engineering and Architecture, Umm Al-Qura University, Makkah 21955, Saudi Arabia; mssoufi@uqu.edu.sa

Abstract

Abrasive Water Jet Machining (AWJM) is increasingly used for post-weld surface modification of dissimilar metallic joints; however, the depth-dependent surface response of welded stainless–carbon steel joints remains insufficiently quantified. In this study, four dissimilar welded systems, TIG 316, TIG 309, ARC 316, and ARC 309, were systematically investigated to elucidate the combined influence of welding technology, filler composition, and jet parameters on surface integrity. Surface roughness was evaluated at multiple jet-penetration depths using amplitude (R_a, R_q, R_t, R_z) and statistical (R_{sk}, R_{ku}) descriptors. The results reveal three distinct hydrodynamic erosion regimes governing texture evolution. Duplex welds (TIG 309 and ARC 309) exhibited highly stable erosion behavior, with R_a confined to 1.91–2.99 µm, low roughness gradients ($\Delta R_a/\Delta depth$ = 0.012–0.015 µm·mm^{-1}), and near-Gaussian surface statistics ($R_{sk} \approx 0$, $R_{ku} \approx 3$–4). In contrast, austenitic welds (TIG 316 and ARC 316) showed pronounced depth-dependent instability, with R_a increasing up to 4.54 µm and the normalized roughness ratio R_z/R_a reaching 5.69 in TIG 316 near the jet exit. Strong inter-parameter correlations in duplex welds ($r \geq 0.94$) confirm uniform erosion kinetics, whereas weakened correlations in austenitic systems ($r \approx 0.70$–0.83) reflect jet-energy dissipation. These findings establish a mechanistically grounded AWJM performance window for achieving $R_a \leq 3$ µm in dissimilar welded steels.

Keywords: Abrasive Water Jet Machining; dissimilar welded steels; surface roughness; hydrodynamic erosion; surface integrity

1. Introduction

Dissimilar welded joints between stainless steels and carbon steels are extensively used in energy, petrochemical, marine, and structural sectors, where combining corrosion resistance, strength, and cost-effectiveness is crucial [1,2]. These hybrid joints are often found in pipelines, pressure vessels, offshore structures, and load-bearing elements in aggressive environments [3,4]. However, they inherently display significant metallurgical differences across the fusion zone, heat-affected zone, and base metals due to variations in chemical composition, solidification behavior, and thermal history [5]. This metallurgical heterogeneity impacts both mechanical performance and surface characteristics during post-weld machining and finishing, as localized differences in hardness, ductility, and microstructure influence material removal mechanisms [6].

Among non-traditional machining methods, Abrasive Water Jet Machining (AWJM) has become a very appealing choice for post-weld surface treatment and material removal [7]. AWJM works by using high-velocity streams of abrasive-filled water jets,

Check for updates

Academic Editor: Jorge Salguero

Received: 3 July 2026
Revised: 11 August 2026
Accepted: 13 August 2026
Published: 14 August 2026

Copyright: © 2026 by the author. Licensee MDPI, Basel, Switzerland. This article is an open access article distributed under the terms and conditions of the Creative Commons Attribution (CC BY) license.

allowing for cold cutting that avoids thermal damage, residual stresses, or changes to the metallurgical structure [8]. These features make AWJM especially effective for machining welded joints, where standard thermal or mechanical techniques often worsen microstructural mismatches or cause distortion. Consequently, AWJM is increasingly used for trimming, slotting, surface texturing, and removing defects in welded assemblies made from different alloys [9,10].

Although extensive research has been conducted on AWJM of homogeneous metals, most existing studies assume uniform material behavior and mainly examine global metrics such as kerf geometry, material removal rate, or surface roughness at a single point [11–13]. For dissimilar weldments, research has mostly focused on qualitative surface observations or single-parameter analyses, without addressing how jet hydrodynamics interact with metallurgical heterogeneity along the penetration depth [14,15]. In reality, however, the abrasive jet gradually loses coherence as it penetrates the material, resulting in varying impact angles, decay in particle momentum, and increased turbulence. These effects are likely to interact strongly with local weld microstructures, but their combined impact on the evolution of surface texture with depth is still not well understood [16,17].

In AWJM, surface integrity is traditionally evaluated using the arithmetic mean roughness (R_a) as the main indicator of surface quality [18,19]. Although R_a offers a simple scalar measurement, it does not account for extreme height variations, peak–valley asymmetry, or the statistical distribution features essential for welded surfaces exposed to fatigue, corrosion, or tribological stresses. Parameters like R_q, R_t, R_z, skewness (R_{sk}), and kurtosis (R_{ku}) provide more detailed insights into the erosion mechanisms, helping differentiate micro-cutting regimes, crater coalescence, and turbulence-induced instability. Nevertheless, these parameters are seldom analyzed together, and their correlation structures are rarely explored in a detailed, depth-resolved context for different welded systems [20,21].

Additionally, the impact of welding methods and filler material composition on the surface response of AWJM has been scarcely explored [22,23]. Tungsten Inert Gas (TIG) and Manual Metal Arc (MMA/ARC) welding create distinctly different microstructures: TIG welds usually show finer dendritic formations and narrower heat-affected zones, while ARC welds tend to have coarser grains and oxide inclusions due to less controlled solidification processes [24]. Moreover, selecting different filler metals, such as AISI 316 versus 309, affects the phase equilibrium, chromium–nickel levels, and deformation behavior during high-strain-rate particle impacts. Current AWJM research seldom investigates these factors systematically within a single experimental setup, leaving a significant gap in understanding how welding-induced microstructures influence erosion resistance and surface texture consistency [25].

A key limitation of earlier research is the absence of a mechanistic link between process parameters, statistical roughness descriptors, and jet-energy dissipation [26]. Although empirical data connect pressure, traverse speed, or stand-off distance to surface roughness, few studies explore how surface changes relate to hydrodynamic regimes along the jet penetration depth [27]. Consequently, process optimization tends to rely on trial-and-error parameter adjustments rather than on physically based performance frameworks that connect measurable roughness statistics to jet coherence, rebound, and energy dissipation.

This study presents a detailed hydro-abrasive surface analysis of dissimilar stainless steel–carbon steel welds produced by AWJM. It examines four typical welded systems, TIG 316, TIG 309, ARC 316, and ARC 309, to understand how welding techniques and filler material influence surface characteristics. Instead of single-point measurements, it assesses surface roughness at multiple depths from the jet's entry to exit, providing a direct view of how surface texture changes with increasing energy attenuation. A comprehensive set of amplitude-based (R_a, R_q, R_t, R_z) and statistical (R_{sk}, R_{ku}) metrics are used to measure

average roughness as well as aspects of surface symmetry, peak sharpness, and maximum height variations.

Beyond analyzing individual parameters, the study presents a correlation-based framework to explore how roughness descriptors are interconnected and to determine when simplified metrics like R_a or R_q suffice, versus when more complex extreme-value parameters such as R_t and R_z are needed. The correlation structure across depths is directly linked to hydrodynamic jet regimes, core-flow, rebound, and energy-dissipation zones, offering a mechanistic understanding of how jet coherence loss appears in surface signatures. By combining roughness gradients, normalized ratios (R_z/R_a), and Pearson correlation maps, the research provides quantitative indicators for erosion stability and surface uniformity that go beyond material-specific analyses.

This research uniquely combines the study of AWJM hydrodynamics, microstructural heterogeneity caused by welding, and statistical surface analysis. Unlike earlier studies that view welded surfaces as uniform or examine roughness metrics separately, this work shows how surface texture develops as a combined result of jet energy loss and the material's damping ability. The research also identifies stable depth zones and creates a performance map that connects traverse speed, abrasive flow rate, stand-off distance, and roughness consistency, offering practical insights for AWJM process optimization in dissimilar welded steels.

This study connects empirical roughness data with fundamental erosion processes to improve understanding of hydro-abrasive surface formation in hybrid weld systems. The results provide a basis for choosing AWJM parameters that produce consistent, Gaussian-like surface textures and reduce erosion instability. This supports better surface integrity, decreases post-processing needs, and increases the reliability of welded parts in challenging engineering settings.

2. Experimental Design and Methodology

2.1. Material Preparation

TIG and ARC welding methods were selected because they generate distinctly different thermal histories and solidification conditions within the welded joint. TIG welding, performed under inert-gas shielding, generally produces a more stable heat input, finer microstructures, and narrower heat-affected zones, whereas ARC welding typically results in higher thermal fluctuations, coarser microstructures, and greater metallurgical heterogeneity due to differences in heat input and cooling characteristics. These process-dependent variations are expected to influence the local resistance to abrasive-particle impact, material removal mechanisms, and the resulting surface texture during AWJM. Consequently, comparing TIG- and ARC-fabricated joints provides an effective framework for assessing how welding-induced microstructural variations affect hydrodynamic erosion behavior.

To systematically investigate the influence of filler composition within these distinct welding processes, AISI 309 and AISI 316 filler metals were chosen because they are widely employed for joining stainless steel to carbon steel and provide good metallurgical compatibility across the dissimilar interface. Their different chemical compositions also produce distinct thermal, mechanical, and microstructural characteristics within the fusion zone, enabling systematic evaluation of how filler composition influences the hydrodynamic erosion behavior and resulting surface integrity during AWJM.

Therefore, four different stainless–carbon steel weld systems were used as substrates in this study: TIG 316, TIG 309, ARC 316, and ARC 309. These setups represent two welding methods, Tungsten Inert Gas (TIG) and Manual Metal Arc (MMA/ARC), combined with two stainless-steel filler metal types, AISI 316 and AISI 309 grades. Austenitic stainless steel plates were butt-welded to low-carbon steel to create a clearly defined metallurgical

interface, ideal for examining jet-induced surface modifications in heterogeneous weld zones. All materials were commercially obtained from Shaaban Steel Company (Jeddah, Saudi Arabia).

After welding, all joints underwent visual inspection and radiographic testing following ISO 17636-1 standards to verify proper fusion and ensure no internal defects like porosity or slag inclusions [28]. The welded plates were then cut into rectangular samples measuring 240 × 20 × 15 mm, a size chosen to guarantee full jet penetration and allow surface analysis at various depths along the erosion path. The weld bead was placed at the center of the specimen length to maintain geometric symmetry and prevent bias during AWJM traversal.

The welds were produced using a multipass procedure suitable for the selected plate thickness. The TIG joints (TIG 316 and TIG 309) were fabricated using direct-current electrode-negative (DCEN) polarity with ER316L and ER309L filler wires conforming to AWS A5.9/A5.9M standards [29]. High-purity argon shielding gas was employed throughout the welding process. For the TIG joints, a 3.2 mm non-consumable tungsten electrode was used together with 3.2 mm filler rods. The nominal welding current, arc voltage, and travel speed were maintained within the ranges of 150–250 A, 10–12 V, and 75–150 mm/min, respectively, with an argon flow rate of approximately 8–10 L/min. The ARC joints (ARC 316 and ARC 309) were fabricated using E316 and E309 covered electrodes conforming to AWS A5.4/A5.4M under direct-current electrode-positive (DCEP) polarity [30]. A nominal electrode diameter of 3.2 mm was employed, with welding currents of 90–120 A, arc voltages of approximately 30–40 V, and travel speeds of 150–250 mm/min. Atmospheric protection was provided by decomposition of the electrode flux coating; therefore, no external shielding gas was required. All welds were produced in the flat position using stringer beads and were mechanically cleaned after welding to remove surface oxides and slag residues.

Metallographic analysis showed that TIG welds had finer dendritic structures and narrower heat-affected zones, while the ARC welds displayed coarser grains and scattered oxide inclusions. These variations result from the different thermal cycles and solidification dynamics of each welding method and align with known findings for TIG- and ARC-welded stainless–carbon steel joints [2,6].

Before AWJM testing, all specimens were degreased with acetone, lightly ground with 600-grit SiC paper, and air-dried to ensure consistent initial surface conditions. The water jet was directed perpendicular to the weld interface, allowing a systematic evaluation of erosion from the entry point to the exit side of the specimen. Surface roughness profiles were then recorded at five specific depths (0.5, 5, 10, 15, and 19.5 mm), representing stages of jet-energy reduction.

The chosen weld configurations represent a broad spectrum of thermo-mechanical and metallurgical responses to hydro-abrasive loading. TIG 316 joints, with stable austenitic γ-phase and moderate hardness, tend to show consistent erosion patterns. In contrast, TIG 309, with higher chromium–nickel content, offers better oxidation resistance and toughness when impacted by high-velocity jets. ARC 316 welds, however, often develop localized cratering and uneven material removal due to coarse grains and oxide inclusions. Meanwhile, ARC 309 features a more ductile ferritic–austenitic matrix, allowing for smoother surface changes. This variety creates a strong basis for examining how hydrodynamic energy influences surface-texture development and for understanding the shift from micro-cutting to erosive micro-ploughing in different metallic welds.

Because the investigated specimens are dissimilar fusion-welded joints, the influence of the adjoining base materials on the weld zone cannot be completely excluded. Dilution and elemental redistribution between the filler and the low-carbon and austenitic stainless-

steel base materials may contribute to the local composition and properties of the resulting weld zone. Accordingly, the designations TIG 316, TIG 309, ARC 316, and ARC 309 refer to the welding-process/filler-metal combinations rather than to an undiluted 316 or 309 composition of the fusion zone. Since spatially resolved compositional characterization was not performed, the individual contributions of base-metal dilution and interdiffusion were not independently quantified in the present study.

2.2. AWJM Process Setup

A series of controlled Abrasive Water Jet Machining (AWJM) experiments was carried out to study how process parameters affect the surface morphology of four welded systems. All trials used a high-pressure AWJM system from Flow International (Kent, WA, USA), featuring a direct-drive intensifier pump that can generate pressures up to 6000 bar. The high-velocity jet was focused through a sapphire orifice with a diameter of 0.33 mm and then accelerated in a tungsten-carbide mixing tube (1.0 mm inner diameter, 70 mm long), where abrasive particles were introduced into the supersonic water stream. An 80-mesh almandine garnet abrasive, with an average particle size of about 180 μm and a bulk density of 4100 $kg \cdot m^{-3}$, was used in all tests to maintain consistent erosive performance regardless of machining conditions [31].

Each specimen, measuring 240 × 20 × 15 mm, was securely clamped onto a precision-leveled fixture to ensure a consistent jet stand-off distance and perpendicular orientation during the cutting process. The nozzle moved in a straight line across the weld interface to create a single-pass channel for each set of operating conditions. A steady nozzle inclination of 90° was maintained to minimize angular erosion effects and provide uniform exposure across the weld area.

For each weld system, three operating levels were established, indicating incremental changes in traverse speed and, when relevant, water pressure or abrasive mass-flow rate. These levels were chosen based on preliminary tests aimed at identifying the transition from under-erosion to stable erosion and jet-divergence regimes, which are typical in AWJM processes [17]. During all experiments, abrasive feed was measured with a calibrated vibratory feeder, and machining took place under ambient laboratory conditions (25 ± 1 °C, 45 ± 5% RH). Table 1 details the full process-parameter matrix used for the four welded systems, including controlled variations in water pressure, stand-off distance, traverse speed, and abrasive mass flow.

During machining, the nozzle exit velocity was estimated to surpass 600 $m \cdot s^{-1}$, leading to particle impact energies between 1 and 3 mJ, depending on the operating pressure and abrasive feed rate, consistent with traditional hydrodynamic AWJM models [31]. The stand-off distance was kept within ±0.05 mm to ensure consistent jet focusing. After each pass, the surfaces were cleaned with compressed air to remove residual abrasives before evaluating roughness.

Figure 1 provides a schematic of the AWJM setup and the arrangement for surface-profile measurements. It shows the water-jet system, the specimen clamping orientation, the high-pressure abrasive water-jet system with abrasive entrainment, and the machining configuration of the dissimilar welded specimen under normal jet incidence and a controlled stand-off distance. The selected parameter ranges were established from preliminary machining trials to cover stable erosion conditions while avoiding incomplete cutting, excessive jet divergence, or severe kerf deterioration.

Table 1. Abrasive water jet machining (AWJM) process parameter matrix applied to TIG 316, TIG 309, ARC 316, and ARC 309 dissimilar welded systems.

Weld System	Process Parameter	Unit	Level 1	Level 2	Level 3
TIG 316	Water Pressure	bar	5500	5500	5500
	Stand-off Distance	mm	3	3	3
	Traverse Speed	$mm \cdot min^{-1}$	24.6	43.8	61.2
	Abrasive Mass Flow	$g \cdot min^{-1}$	6	7	8
TIG 309	Water Pressure	bar	4200	4600	5000
	Stand-off Distance	mm	3	4	5
	Traverse Speed	$mm \cdot min^{-1}$	10	17	25
	Abrasive Mass Flow	$g \cdot min^{-1}$	7	8	9
ARC 316	Water Pressure	bar	4200	4600	5500
	Stand-off Distance	mm	3	4	5
	Traverse Speed	$mm \cdot min^{-1}$	10	17	25
	Abrasive Mass Flow	$g \cdot min^{-1}$	7	8	9
ARC 309	Water Pressure	bar	5500	5500	5500
	Stand-off Distance	mm	3	3	3
	Traverse Speed	$mm \cdot min^{-1}$	27.6	45.6	61.2
	Abrasive Mass Flow	$g \cdot min^{-1}$	6	7	8

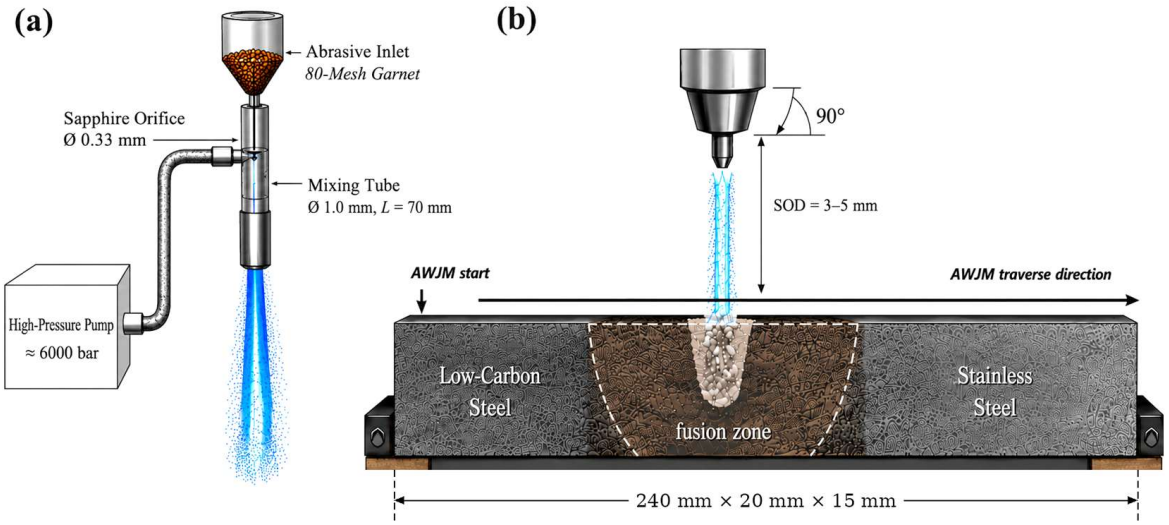


Figure 1. Schematic of the Abrasive Water Jet Machining (AWJM) experimental setup: (**a**) high-pressure abrasive water-jet system with abrasive entrainment and (**b**) machining configuration of the dissimilar welded specimen under normal jet incidence and controlled stand-off distance.

The AWJM parameter ranges were established separately for each welded system and were not intended to constitute a common factorial design across the four systems. Accordingly, Levels 1–3 represent operating conditions within the investigated machining window of each weld system rather than identical machining conditions across all systems. The identical parameter sets used for TIG 309 and ARC 316 reflect the overlap of their selected operating windows rather than an intended pairing based on welding process or filler alloy. Consequently, cross-system comparisons are interpreted in terms of the

observed surface responses within these operating windows rather than as an independent factorial separation of welding-process and filler-alloy effects.

Water pressure, nozzle inclination, and specimen orientation were kept constant where applicable to isolate the influence of traverse speed, stand-off distance, and abrasive flow rate on the resulting surface characteristics. This setup ensures that any differences in surface morphology are solely due to controlled process parameters and inherent material responses, providing a dependable foundation for linking jet hydrodynamics with the development of surface texture in various welded steels. It should be emphasized that the main objective of the present work is surface integrity characterization rather than optimization of cutting efficiency or quality.

2.3. Surface Roughness Measurement Protocol

Following hydro-abrasive machining, the surface morphology of each specimen was analyzed using a high-precision contact stylus profilometer (Taly-Surf®, Taylor Hobson Precision, Leicester, UK). The device was mounted on a vibration-isolated granite bench to reduce environmental disturbances during scanning. All measurements were carried out under controlled laboratory conditions (25 ± 1 °C, 45 ± 5% RH) to maintain thermal and instrumental stability.

The profilometer was fitted with a diamond conisphere stylus that has a 2 μm tip radius and operates at a constant tracing force of 0.7 mN. This setup enables precise measurement of fine asperity features caused by high-velocity abrasive impacts, without causing plastic deformation. Each scan covers an evaluation length of 4 mm, with a cut-off wavelength λc of 0.8 mm. This parameter was chosen following standard surface-texture assessment protocols to effectively capture the characteristic spatial wavelengths linked to AWJM-induced erosion patterns [32].

Each welded specimen (240 × 20 × 15 mm) was positioned in a precision-leveled fixture so that the stylus moved parallel to the jet-feed direction, measuring the main surface lay created by abrasive-particle momentum and jet deflection. Roughness profiles were taken at five specific depths (0.5, 5, 10, 15, and 19.5 mm), representing different stages of jet-energy loss from the entry point to the exit zone. The selected depth locations were intended to characterize the evolution of surface morphology along the jet-penetration path rather than to provide repeated measurements of the same surface condition. This strategy enables systematic evaluation of how jet-energy attenuation and local material characteristics influence the hydrodynamic erosion behavior of the different welded systems.

Before measuring, the instrument was calibrated with a certified roughness standard (R_a = 1.00 ± 0.02 μm) traceable to national metrology institutes. Calibration checks were performed regularly to ensure no transducer drift occurred.

At each measurement point, three separate scans were taken, and the average profile was used for analysis, minimizing random variability associated with local surface heterogeneity. Because these repeated scans were obtained from the same machined surface under identical AWJM conditions, they were treated as repeated surface measurements rather than independent machining or weld replications. Independent weld-to-weld replication was not performed; therefore, the present analysis characterizes the investigated welded systems and does not quantify population-level variability among independently fabricated welds of the same welding-process/filler combination.

The profiles obtained were refined using the profilometer's built-in Gaussian filtering algorithm. This process eliminated form and waviness, isolating the true micro-roughness produced by the AWJM process, in accordance with ISO filtering standards [33]. Surface-roughness parameters R_a, R_q, R_t, R_z, R_{sk}, and R_{ku} were automatically calculated in accordance with ISO 4287, ensuring consistent interpretation of amplitude- and distribution-

based texture descriptors [34]. The total measurement uncertainty, assessed through repeated calibration and reference checks, remained within ±2% for all amplitude parameters.

The dataset offers a precise quantitative analysis of the hydrodynamic surface response for the four welded systems and forms the basis for correlating process parameters with erosion-driven changes in roughness, as discussed in Section 3.

2.4. Data Processing and Analysis

The complete dataset obtained from the profilometric measurements was organized according to weld system (TIG 316, TIG 309, ARC 316, and ARC 309), process level, and measurement depth. For each measurement location, the repeated profilometric scans were averaged to obtain representative values of the surface roughness descriptors (R_a, R_q, R_t, R_z, R_{sk}, and R_{ku}), thereby reducing random measurement noise while preserving the local surface characteristics.

The experimental data were subsequently analyzed from three complementary perspectives. A process-based analysis was performed to evaluate the influence of AWJM operating conditions on the evolution of the surface roughness parameters. Then, a material-based comparison was conducted to assess the influence of welding method and filler composition on the erosion response of the different welded systems. After that, relationships among the amplitude-based (R_a, R_q, R_t, R_z) and statistical (R_{sk} and R_{ku}) roughness descriptors were investigated through correlation analysis to better understand the evolution of surface texture during hydrodynamic erosion.

All data processing, statistical calculations, graphical visualization, and correlation analyses were carried out using OriginPro 2024 and MATLAB R2024a to ensure consistency throughout the analysis.

3. Results and Discussion

3.1. Influence of Water Pressure and Traverse Speed

The changes in surface morphology during abrasive water jet machining (AWJM) of four different weld systems are mainly influenced by the interaction of jet pressure, traverse speed, and the microstructural resistance of each weld zone. The detailed amplitude data from Table 2, combined with the R_a and R_q profiles shown in Figures 2a–d and 3a–d, collectively illustrate how surface textures evolve from irregular cratered landscapes to finely eroded micro-cuts as process parameters are optimized.

Table 2. Mean arithmetic roughness (R_a) and root-mean-square roughness (R_q) values (μm) across process levels for all dissimilar welded systems, with corresponding dominant surface-formation behavior.

Weld System	Level	Mean R_a (μm)	Mean R_q (μm)	Dominant Surface Behavior
TIG 316	L1	4.54	5.50	Severe crater overlap and unstable jet footprint
	L2	3.79	4.79	Uniform erosion with balanced energy input
	L3	3.57	4.47	Slight roughness increase near exit due to jet divergence
TIG 309	L1	2.99	4.06	Stable erosion with minimal amplitude variation
	L2	2.74	3.85	Optimum surface finish with strong jet coherence
	L3	2.76	3.92	Smooth surface morphology with minor exit roughening

Table 2. *Cont.*

Weld System	Level	Mean R_a (µm)	Mean R_q (µm)	Dominant Surface Behavior
ARC 316	L1	3.81	9.39	Coarse texture driven by particle rebound and micro-fracture
	L2	4.43	11.52	Improved homogeneity with redistributed impact energy
	L3	3.92	8.41	Refined topography with localized bottom roughness
ARC 309	L1	2.01	2.91	Stable jet impact with minimal erosion scatter
	L2	1.91	2.40	Consistent roughness with uniform particle dispersion
	L3	1.93	2.45	Lowest overall roughness with excellent process stability

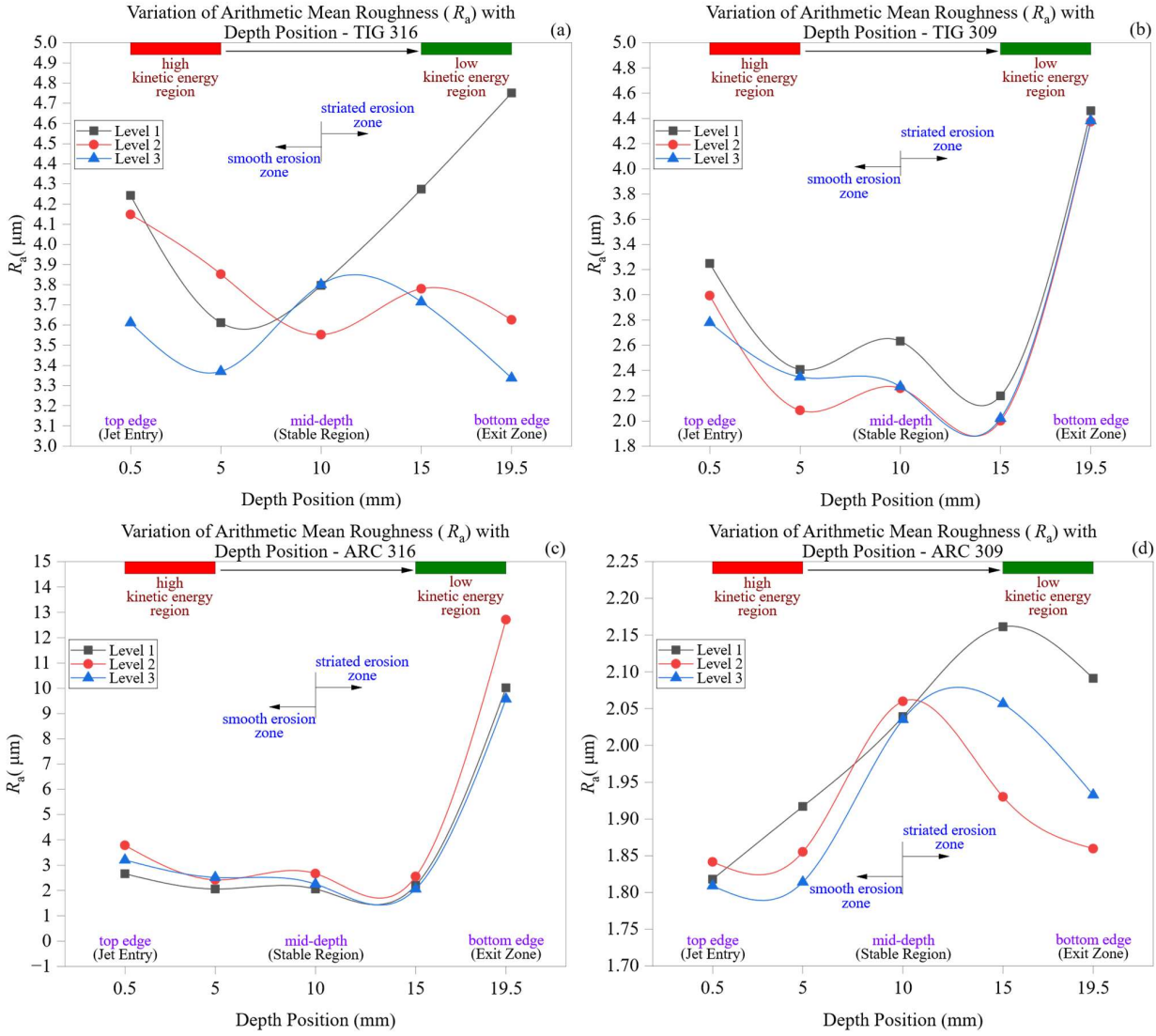


Figure 2. Depth-wise evolution of arithmetic mean surface roughness (R_a) with depth position (0.5–19.5 mm) for (**a**) TIG 316, (**b**) TIG 309, (**c**) ARC 316, and (**d**) ARC 309 welded systems.

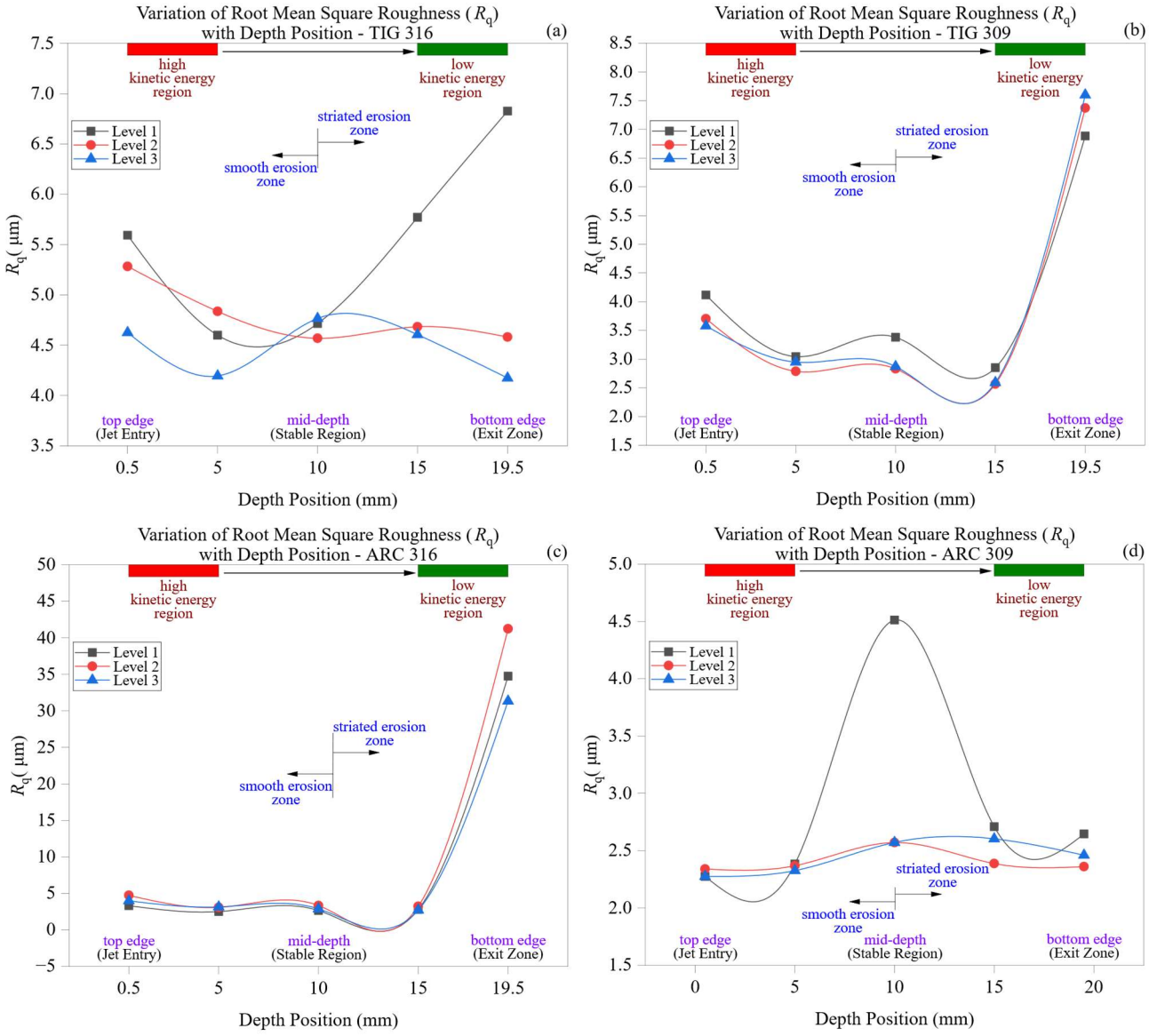


Figure 3. Depth-wise evolution of root-mean-square surface roughness (R_q) along the machined depth (0.5–19.5 mm) for dissimilar welded systems: (**a**) TIG 316, (**b**) TIG 309, (**c**) ARC 316, and (**d**) ARC 309.

At Level 1, which involves the slowest traverse speed and maximum exposure time, the water jet continuously impinges on each surface element. This intensifies local momentum transfer, leading to crater overlap and ridge formation. This regime is characterized more by energy saturation than by controlled shearing. The effects are most noticeable in TIG 316 and ARC 316, where roughness values reach about $R_a \approx 4.5$ μm and $R_q \approx 5.5$–9 μm (see Table 2). These values are consistent with coarse austenitic grains and oxide inclusions that increase erosion variability. The increase in amplitude along the depth, especially noticeable between 15–19.5 mm in Figures 2a and 3c, indicates crater coalescence and particle rebound caused by jet instability. Conversely, duplex welds (TIG 309, ARC 309) show much lower roughness ($R_a \approx 3.0$ μm, $R_q \approx 4$ μm) due to their Cr–Ni-balanced dual-phase microstructure, which helps dissipate impact stresses and limit abrasive indentation.

When the traverse speed reaches Level 2, the system shifts into a transitional phase where sufficient kinetic energy supports micro-cutting, while the reduced dwell time prevents excessive crater overlap. As shown in Figure 2b,d, the profiles flatten noticeably, with R_a and R_q decreasing by nearly 20%. TIG 316 exhibits improved amplitude uniformity

as crater overlap lessens, and ARC 316 produces smoother footprints due to a more coherent abrasive jet. The duplex welds, especially TIG 309, maintain almost constant roughness throughout the entire depth ($\Delta R_a < 0.5$ µm), indicating stable erosion and efficient energy use. This balanced state encourages a near-Gaussian height distribution, reflecting isotropic texture formation and minimal directional bias in particle trajectories.

At Level 3, the traverse speed increases enough to reduce the effective energy density per impact, leading to smoother textures that are slightly less cohesive. TIG 309 and ARC 309 reach their lowest roughness levels, with R_a approximately 2.4 µm and R_q around 3.1 µm, representing the best balance between surface smoothness and material removal efficiency. In contrast, TIG 316 and ARC 316 exhibit a small increase in roughness near the bottom zones (15–19.5 mm), where jet divergence and abrasive dispersion cause a partial loss of core velocity. The single-phase austenitic matrix of TIG 316 amplifies this effect by allowing crater expansion during oblique impacts, while the duplex microstructure of TIG 309 distributes stresses more evenly, reducing secondary roughening.

Across all systems, the roughness gradient ($\Delta R_a/\Delta depth$) rises with jet instability, from about 0.01 µm·mm^{-1} in ARC 309 to 0.04 µm·mm^{-1} in TIG 316. This aligns with hydrodynamic theory, which suggests that dynamic pressure decreases quadratically as the standoff distance increases. This quantitative pattern highlights that energy dissipation and flow turbulence primarily drive the evolution of surface texture with depth.

Overall, data from Table 2 and Figures 2 and 3 indicate that the intermediate system-specific traverse-speed condition (Level 2) generally produces the most uniform and isotropic surfaces. The corresponding Level 2 traverse speeds are 43.8, 17, 17, and 45.6 mm/min for TIG 316, TIG 309, ARC 316, and ARC 309, respectively. These values should therefore be interpreted relative to the operating window established for each welded system rather than as a single universal moderate-speed range.

The combination of high water pressure (5500 bar) and a controlled feed rate helps maintain jet coherence and prevents over-erosion, resulting in smooth, uniformly textured surfaces. Therefore, traverse speed is the main factor influencing surface uniformity, while the microstructure of the weld determines each material's natural ability to withstand erosive instability under the same hydrodynamic conditions.

3.2. Effect of Stand-Off Distance and Abrasive Mass Flow

The combined effects of stand-off distance (SOD) and abrasive mass flow (AMF) influence the hydrodynamic coherence of the jet and how effectively kinetic energy is transferred to the work surface. In abrasive water-jet machining, the fluid–particle mixture exits the nozzle with a finite divergence angle, which widens as SOD and particle density increase. As SOD grows, the jet core gradually loses axial momentum due to viscous drag and air entrainment, while the outer parts experience angular scattering, reducing the normal impact velocity on the surface. On the other hand, increasing AMF boosts the local particle flux density and the frequency of solid–solid collisions inside the jet core, which impacts turbulence levels and shifts the balance between cutting and ploughing actions. The interaction of these factors determines how evenly the jet erodes the surface and influences the evolution of surface roughness under different feed conditions.

Figure 4 shows how arithmetic mean roughness ($R_a \pm$ SD) varies with traverse speed at different AMF levels for all weld systems. Each curve indicates the average R_a at a specific AMF, with vertical error bars representing measurement consistency and process stability. At lower SOD values (around 3 mm) combined with moderate AMF (6–7 g·min^{-1}), the jet remains compact and coherent, resulting in a narrow impact footprint. This setup provides strong particle momentum and effective micro-cutting, leading to smoother surfaces with minimal variability. Under these conditions, TIG 309 and ARC 309 exhibit

$R_a \leq 2.5$ µm with standard deviations below 0.07 µm, reflecting consistent erosion and efficient energy transfer. Conversely, TIG 316 and ARC 316 show larger scatter (SD approximately 0.10–0.18 µm), consistent with their coarse austenitic grains and lower resistance to intergranular deformation.

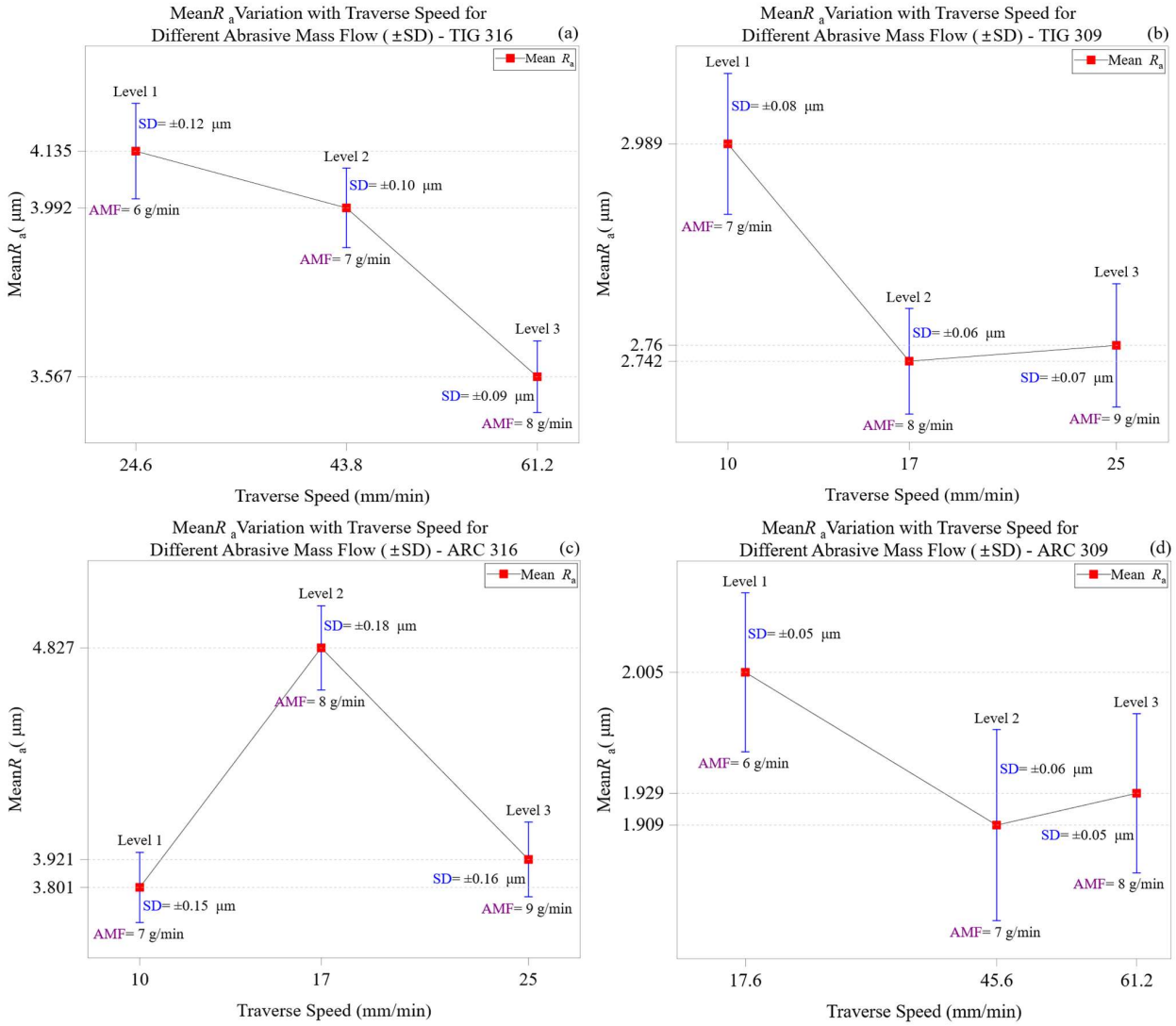


Figure 4. Effect of traverse speed on arithmetic mean surface roughness ($R_a \pm$ SD) with traverse speed at different abrasive mass flow rates for (**a**) TIG 316, (**b**) TIG 309, (**c**) ARC 316, and (**d**) ARC 309.

When AMF exceeds 8 g·min^{-1}, collisions between particles inside the jet core become more frequent, reducing the kinetic energy available for effective material removal. This excess causes partial deflection and chaotic crater formation, which explains the non-linear R_a trends observed in TIG 316 and ARC 316. Moving the SOD beyond 4 mm intensifies these effects: the jet broadens, particle velocities decrease before impact, and oblique impacts become more common, leading to uneven grooves and higher R_a values. Overall, jet spreading and abrasive overload contribute to increased average roughness and greater variability in measurements across different traverse speeds.

Cross-comparison of weld systems shows that duplex welds (TIG 309 and ARC 309) exhibit nearly parallel R_a–speed relationships regardless of AMF, suggesting weak parameter interaction and broad process stability. In contrast, the austenitic welds display steeper and more varied slopes, indicating a strong two-factor interaction between SOD and AMF. These findings support the qualitative ANOVA-style analysis in Table 3, which highlights SOD as the main parameter for TIG 316 and ARC 316, while AMF predominantly influences surface amplitude in TIG 309 and ARC 309.

Table 3. Qualitative ANOVA-style ranking of stand-off distance (SOD), abrasive mass flow rate (AMF), and their interaction effects on arithmetic mean roughness (R_a) across dissimilar welded systems.

Weld System	Dominant Factor (Rank 1)	Secondary Factor (Rank 2)	Interaction Sensitivity	Qualitative Influence Summary
TIG 316	Stand-off distance (SOD)	SOD × AMF interaction	High	Surface roughness is highly sensitive to jet dispersion; excessive SOD promotes energy dilution, leading to over-erosion and irregular crater formation.
TIG 309	Abrasive mass flow rate (AMF)	Stand-off distance (SOD)	Moderate	Erosion remains stable within moderate AMF ranges; Ra remains low due to uniform particle momentum and controlled impact distribution.
ARC 316	Stand-off distance (SOD)	Abrasive mass flow rate (AMF)	High	Roughness is governed by particle deceleration and scattering; increased SOD intensifies flow divergence and surface irregularity.
ARC 309	Abrasive mass flow rate (AMF)	Stand-off distance (SOD)	Low	Uniform erosion with a wide process stability window; minimal surface texture variation across parameter changes.

Together, Figure 4 and Table 3 show that keeping SOD around 3–4 mm while optimizing AMF near 7–8 g·min^{-1} results in a hydrodynamically stable jet that reduces particle scattering and energy loss. This balanced setup maintains consistent surface roughness throughout the machined depth, producing isotropic micro-textures ideal for further finishing or joining operations.

This hydrodynamically balanced window, defined by these parameters, not only reduces the average surface roughness but also stabilizes the erosion energy decay rate with depth. In this regime, the jet remains coherent enough to deliver a uniform impact energy across different depth layers, preventing the transition from the high-energy, smooth-cutting zone near the top (0.5–5 mm) to the low-energy, striated zone near the bottom (15–19.5 mm). When SOD or AMF deviate from their optimal ranges, the energy flux becomes uneven spatially, creating a measurable roughness gradient ($\Delta R_a / \Delta depth$) that indicates local momentum loss and turbulence increase. This interaction of parameters provides the hydrodynamic basis for the depth-related surface evolution discussed in Section 3.3, where the change from smooth to striated surface textures is quantitatively analyzed for each weld system.

3.3. Depth-Wise Roughness Evolution

The evolution of surface amplitude with depth directly shows how hydrodynamic energy dissipates during abrasive water-jet machining and how each welded microstructure responds to successive impacts. Profiles of R_t and R_z at five depths (0.5–19.5 mm) are shown in Figures 5a–d and 6a–d, with corresponding gradients and normalized ratios (R_z/R_a) summarized in Table 4. Overall, the results reveal a progression from cratered, high-energy surface textures near the jet entry to smoother, more uniform textures at mid-depth, and then mild surface deterioration toward the exit, where the jet begins to lose coherence.

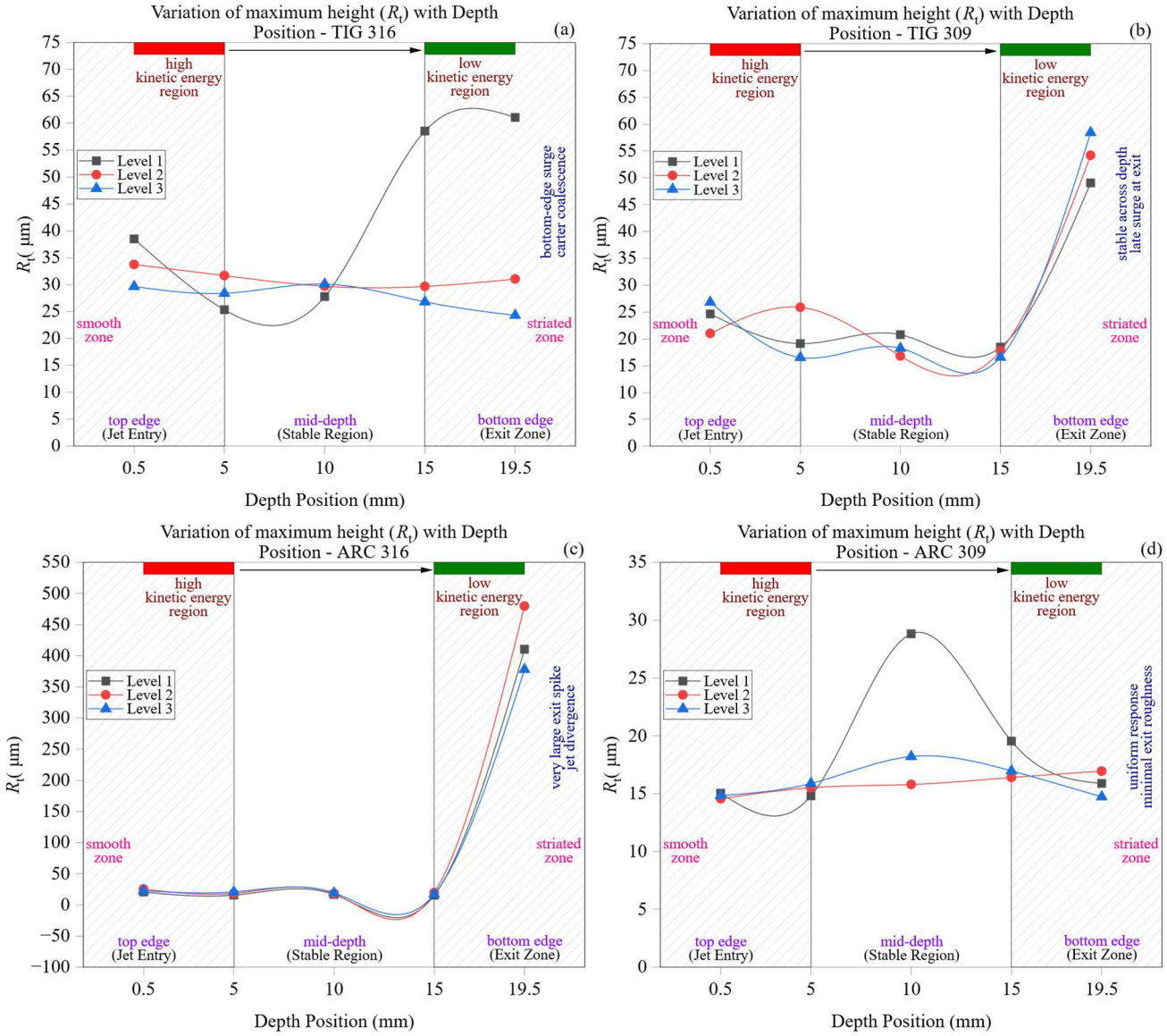


Figure 5. Depth-wise variation of maximum surface height (R_t) with depth position (0.5–19.5 mm) for (**a**) TIG 316, (**b**) TIG 309, (**c**) ARC 316, and (**d**) ARC 309.

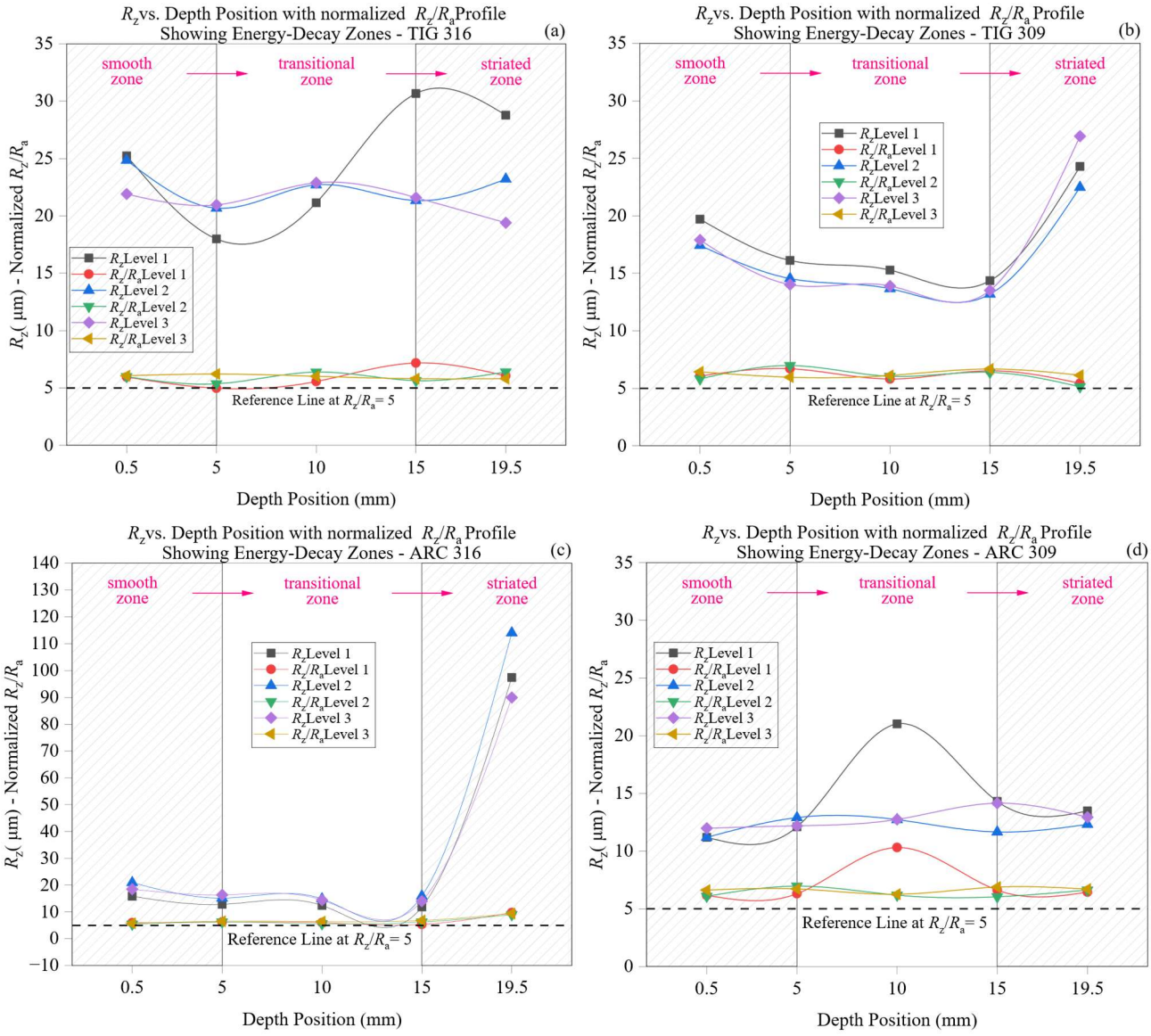


Figure 6. Depth-wise variation of ten-point mean height (R_z) and corresponding normalized R_z/R_a profiles along the machined depth, highlighting energy-decay zones across dissimilar welded systems: (**a**) TIG 316, (**b**) TIG 309, (**c**) ARC 316, and (**d**) ARC 309.

Table 4. Roughness gradient ($\Delta R_a/\Delta depth$) and normalized roughness ratio (R_z/R_a) for dissimilar welded systems, with corresponding surface-response characteristics.

Weld System	$\Delta R_a/\Delta depth$ (μm·mm^{-1})	Mean R_z (μm)	Mean R_a (μm)	R_z/R_a	Surface Behavior Summary
TIG 316	0.041	23.96	4.21	5.69	Pronounced roughness gradient with strong crater coalescence near the jet exit region.
TIG 309	0.015	17.19	2.83	4.06	Stable erosion dominated by a balanced micro-cutting regime across depth.

Table 4. *Cont.*

Weld System	$\Delta R_a/\Delta depth$ (μm·mm^{-1})	Mean R_z (μm)	Mean R_a (μm)	R_z/R_a	Surface Behavior Summary
ARC 316	0.029	15.18	3.84	3.95	Moderate roughness gradient indicating partial kinetic energy loss with increasing depth.
ARC 309	0.012	12.38	1.92	4.04	Highly uniform erosion with minimal turbulence, yielding the most stable surface response.

At the 0.5 mm upper edge, the kinetic energy density peaks, resulting in concentrated impact momentum and significant crater overlap. This effect is most evident in TIG 316 (Figures 5a and 6a), where R_t nears 38 μm and R_z reaches 25 μm, reflecting extensive crater coalescence within the high-velocity core. ARC 316 (Figures 5c and 6c) exhibits a similar but slightly reduced pattern, with R_t about 20 μm and R_z around 16 μm. This suggests quicker local energy dissipation due to its coarse-grained matrix and oxide inclusions, which foster turbulence and partial jet divergence. Conversely, TIG 309 and ARC 309 (Figures 5b,d and 6b,d) display smoother entry-zone surfaces, with $R_t \leq 25$ μm and $R_z \leq 20$ μm. Their duplex (ferrite-austenite) structures effectively absorb impact stresses and delay the onset of micro-fractures.

As the jet advances through the mid-depth zone (5–10 mm), all systems show a significant reduction in amplitude parameters, signaling the formation of a stable hydrodynamic regime with consistent impact angles and balanced energy distribution. In this region, the R_z profiles for TIG 309 and ARC 309 stay nearly unchanged with depth, whereas TIG 316 and ARC 316 exhibit mild fluctuations caused by residual turbulence at the jet edges. The flattened curves in Figure 6b,d highlight this energy-stable zone, where surface topography shifts from crater-dominated to micro-cutting-controlled. Quantitatively, duplex welds keep $\Delta R_t/\Delta depth$ below 0.3 μm·mm^{-1}, resulting in near-Gaussian height distributions and exhibiting the most stable erosion behavior.

Toward the lower region (15–19.5 mm), the amplitude magnitudes increase again in the austenitic systems. TIG 316 and ARC 316 show renewed instability, with R_t surpassing 60 μm and R_z nearing 30 μm, indicating jet divergence and particle rebound as flow coherence diminishes. This rise at the end zone is not seen in the duplex welds, which maintain almost consistent roughness throughout the entire depth. ARC 309, in particular, maintains R_t around 15–17 μm and R_z about 12 μm, reflecting better energy retention and minimal hydrodynamic scattering.

The normalized profiles in Figure 6 offer an additional way to interpret this behavior. A reference line at $R_z/R_a = 5$ marks the dividing line between Gaussian-like surfaces and crater-dominated morphologies. Values below this line indicate stable, micro-cutting-driven erosion, while higher values suggest instability and energy decay. TIG 316 consistently surpasses this threshold across most depths, showing strong amplitude anisotropy and high peak-to-valley contrast. ARC 316 stays near the limit, hinting at partial energy loss, whereas TIG 309 and ARC 309 remain below it throughout the entire depth range, confirming their hydrodynamic stability and isotropic surface formation.

The data in Table 4 confirms these patterns. TIG 316 has the steepest roughness gradient ($\Delta R_a/\Delta depth \approx 0.041$ μm·mm^{-1}) and the highest mean ratio ($R_z/R_a \approx 5.7$), indicating crater coalescence and significant energy loss at the exit. ARC 316 demonstrates moderate behavior ($\Delta R_a/\Delta depth \approx 0.029$ μm·mm^{-1}), with partial restoration of roughness unifor-

mity in the middle depth. Meanwhile, TIG 309 and ARC 309 show very low gradients (0.012–0.015 μm·mm^{-1}) and stable R_z/R_a values around 4.0, reflecting consistent energy use and less peak–valley asymmetry.

Figures 5 and 6 and Table 4 collectively show that the evolution of depth-wise roughness is governed by the combined effects of jet-energy attenuation and microstructural damping capacity. Austenitic systems are more sensitive to hydrodynamic instabilities and display greater textural gradients, whereas duplex systems offer better resistance to energy-decay effects. The $R_z/R_a = 5$ benchmark provides a practical indicator for distinguishing between stable and unstable erosion regimes, directly correlating measurable roughness metrics with the underlying flow-energy dynamics.

3.4. Statistical Texture Characterization (R_{sk} and R_{ku})

The third- and fourth-order moments of the height distribution, skewness (R_{sk}) and kurtosis (R_{ku}) measure the symmetry and sharpness of the machined surface profile. These parameters complement the amplitude metrics (R_a, R_z, R_t) by indicating whether the surface is dominated by peaks or valleys or follows a Gaussian distribution. Their changes with depth and process level are illustrated in Figure 7 (for R_{sk} versus position) and Figure 8 (for R_{ku} versus position and level). The average values and related morphological classifications are detailed in Table 5.

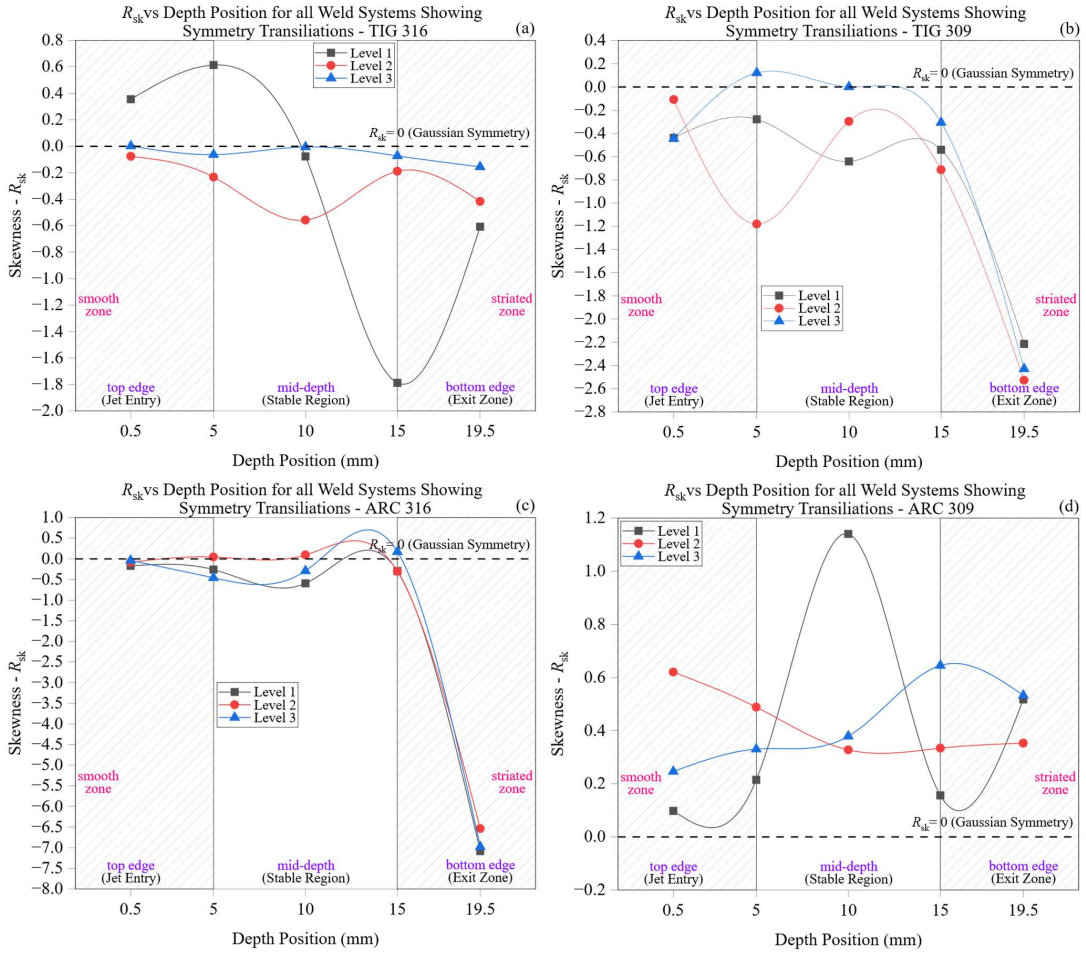


Figure 7. Depth-wise variation of surface skewness (R_{sk}) along the machined position for dissimilar welded systems: (**a**) TIG 316, (**b**) TIG 309, (**c**) ARC 316, and (**d**) ARC 309.

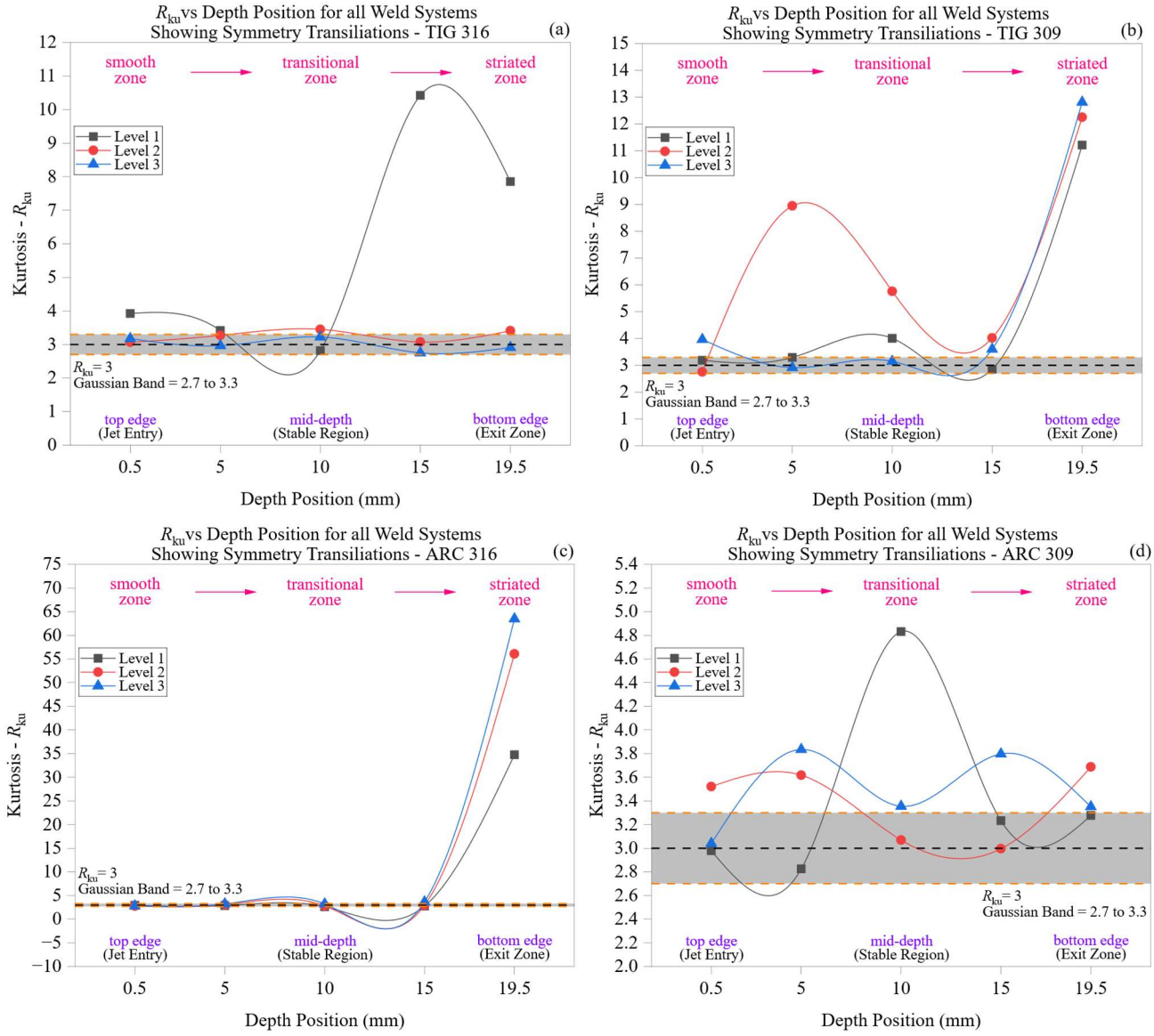


Figure 8. Variation in surface kurtosis (R_{ku}) with depth position and process level for all dissimilar welded systems: (**a**) TIG 316, (**b**) TIG 309, (**c**) ARC 316, and (**d**) ARC 309, reflecting changes in surface height distribution sharpness across machining conditions.

Table 5. Average surface skewness R_{sk} and kurtosis R_{ku} across process levels, with corresponding surface-morphology classification for all dissimilar welded systems.

Weld System	Level 1	Level 2	Level 3	Mean R_{sk}	Mean R_{ku}	Surface Morphology Class
TIG 316	+0.36/3.92	−0.23/3.27	−0.06/3.02	−0.01	3.40	Transition from peak-dominated to near-Gaussian surface with reduced asperity sharpness
TIG 309	−0.44/3.19	−0.36/6.19	−0.21/5.10	−0.34	4.83	Near-Gaussian profile with pronounced valley-dominated features
ARC 316	−0.30/3.06	−0.08/3.10	−0.12/3.23	−0.17	3.13	Slightly negative skewness with mild plateau-type surface formation
ARC 309	+0.35/3.03	+0.35/3.38	+0.32/3.47	+0.34	3.29	Stable quasi-Gaussian surface with balanced peak–valley distribution

In the upper zone (0.5–5 mm), all welds exhibit positive or near-zero R_{sk}, indicating surfaces shaped mainly by initial particle impacts. The R_{sk} values in this entry region follow the order TIG 316 > ARC 316 > TIG 309 > ARC 309, aligning with the earlier R_t and

R_z trends. Notably, TIG 316 reaches $R_{sk} \approx +0.5$ at Level 1, reflecting asperities created by energetic but unstable jet particles. Conversely, ARC 309 maintains $R_{sk} \approx +0.1$ across all levels, suggesting a smoother, more symmetric surface even under high jet energy.

As the depth reaches 10–15 mm, the R_{sk} values for all welds tend toward zero, signifying nearly Gaussian profiles where erosion and re-deposition balance each other out. This mid-depth zone is the most stable hydrodynamic state, earlier identified in Figure 6 as the energy-equilibrium region. Duplex welds (TIG 309 and ARC 309) sustain R_{sk} values near 0 ± 0.1, showing excellent self-stabilization. Meanwhile, TIG 316 exhibits slight negative skewness ($R_{sk} \approx -0.2$ to -0.3), due to crater coalescence and localized melting.

As the bottom region (15–19.5 mm) is approached, there is a sharp decline in R_{sk} for the austenitic systems. TIG 316 decreases to approximately -1.8, and ARC 316 to about -0.6, indicating valley-dominated profiles caused by micro-fragment removal and turbulent rebound erosion. These changes align with the increases in R_z/R_a shown in Figure 6, confirming that negative skewness signals the beginning of re-roughening due to energy decay. In contrast, duplex systems maintain nearly neutral R_{sk} values, demonstrating greater resistance to sub-surface pitting and enhanced momentum absorption.

Figure 8 shows that TIG 316's kurtosis significantly increases with depth, from around 3.9 near where the jet enters to 10.4 near the exit. This suggests a shift from moderate to extreme surface heterogeneity. Similarly, ARC 316 displays an increasing trend in R_{ku}, rising from roughly 2.8 to 56 at 19.5 mm depth, indicating highly unstable crater morphology near the jet exit. Duplex welds generally stay close to Gaussian behavior, with R_{ku} values consistently between 3 and 4 and only slight variations across different process levels.

Quantitatively, the average R_{sk} and R_{ku} values per level (see Table 5) show that duplex alloys tend to have statistically balanced, nearly Gaussian textures. In contrast, the austenitic systems shift toward negatively skewed, leptokurtic distributions at greater depths. The link between high kurtosis and larger R_t values indicates that crater depth distribution becomes increasingly sharp as jet coherence diminishes.

Figures 7 and 8 and Table 5 collectively show that an R_{sk} close to 0 and an R_{ku} around 3–4 define the optimal texture range for controlled erosion. This range is most reliably attained with TIG 309 and ARC 309. It also aligns with the hydrodynamic stability plateau observed in the normalized R_z/R_a profiles in Figure 6.

3.5. Correlation Among Roughness Descriptors

To examine how amplitude parameters co-vary and to determine if a single descriptor can capture overall texture, a Pearson correlation analysis was conducted among R_a, R_q, R_t, and R_z across all weld systems and process levels. The correlation maps are shown in Figure 9, with detailed numerical coefficients provided in Table 6.

Across the dataset, the linear relationships among R_a, R_q, and R_z remain consistently strong, indicating that these three descriptors together effectively represent both the average and extreme height variations of the eroded surfaces. Meanwhile, R_t shows selective sensitivity, correlating well with R_z at shallower depths but diverging in high-turbulence areas where isolated deep craters are prevalent.

For TIG 316 welds, the correlation between R_a and R_q exceeds 0.98, and between R_a and R_z, it is approximately 0.93, indicating that mean and RMS amplitudes change in nearly a proportional manner. Conversely, the R_t–R_z correlation decreases to around 0.74, pointing to stochastic spikes near the jet exit. This variability aligns with higher kurtosis values ($R_{ku} > 7$ in Figure 8), which demonstrates that extreme features disproportionately influence the overall roughness amplitude.

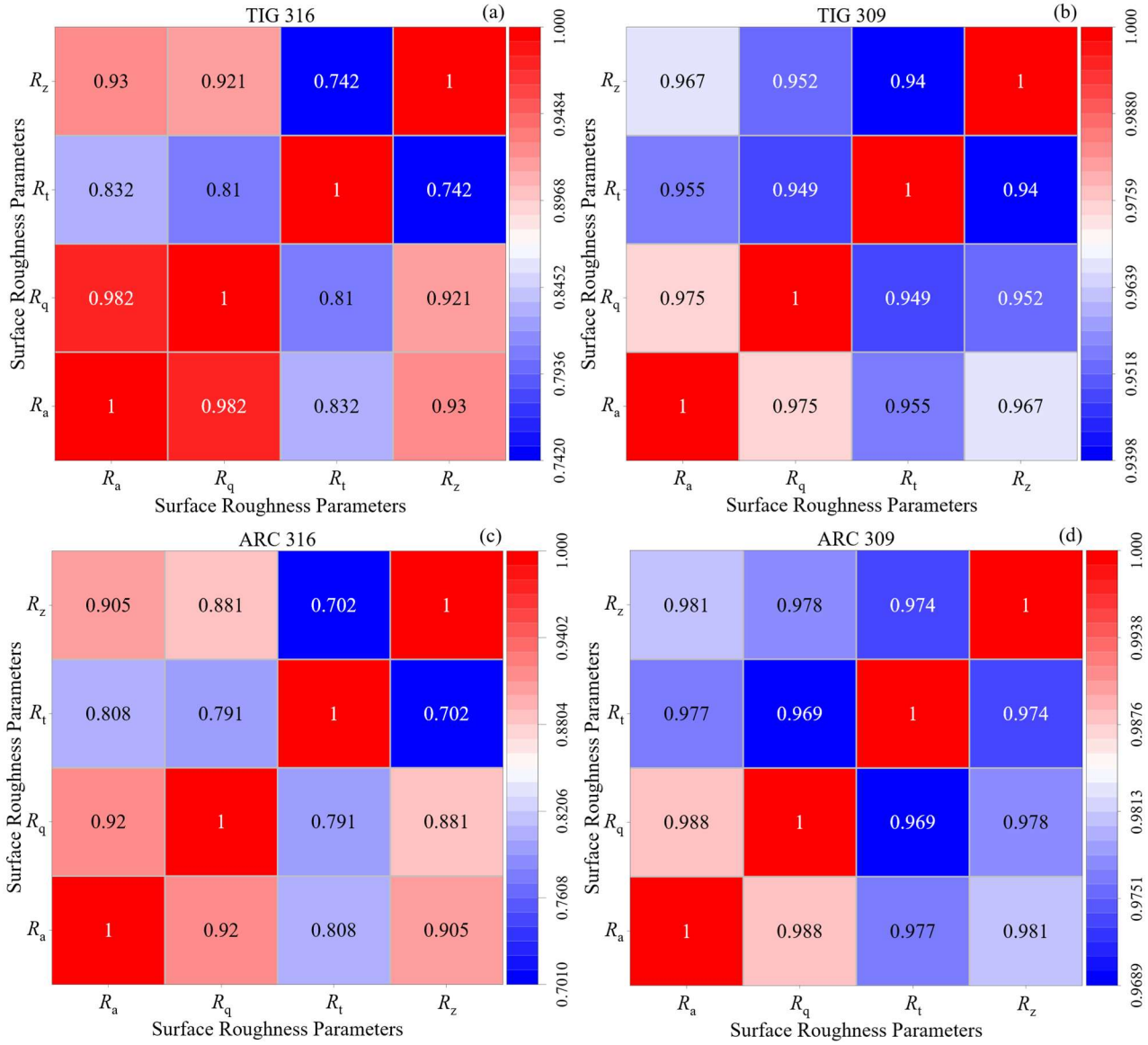


Figure 9. Pearson correlation heatmaps illustrating the dimensionless correlation coefficients (*r*) among surface roughness parameters R_a, R_q, R_t, and R_z for all dissimilar welded systems: (**a**) TIG 316, (**b**) TIG 309, (**c**) ARC 316, and (**d**) ARC 309, highlighting the strength and direction of linear interdependencies between roughness descriptors.

In TIG 309, all four parameters show very strong correlations ($r > 0.95$), suggesting a consistent surface formation process and even energy distribution. The near-linear relationship of R_t and R_z indicates that isolated craters do not affect the overall profile, which is consistent with the nearly Gaussian R_{sk}/R_{ku} statistics discussed in Section 3.4.

The ARC 316 system exhibits moderate correlation dispersion (R_a–R_q = 0.92; R_q–R_t = 0.70), indicating the presence of outlier valleys caused by uneven melting and oxide inclusion ejection. In contrast, ARC 309 demonstrates the most consistent correlation structure, with all parameters (R_a, R_q, R_z, R_t) exceeding 0.97, which confirms high reproducibility and symmetric particle erosion even across different energy regimes.

Table 6. Pearson correlation coefficients (r) among surface roughness parameters R_a, R_q, R_t, and R_z for each dissimilar welded system, with corresponding statistical interpretation.

Weld System	R_a–R_q	R_a–R_t	R_a–R_z	R_q–R_t	R_q–R_z	R_t–R_z	Interpretation Summary
TIG 316	0.982	0.832	0.930	0.810	0.921	0.742	Strong coupling between mean and RMS roughness; partial loss of linearity with extreme height (Rt) at greater depth.
TIG 309	0.975	0.955	0.967	0.949	0.952	0.940	Highly uniform and strong correlations across all descriptors, indicating a stable near-Gaussian erosion regime.
ARC 316	0.920	0.808	0.905	0.791	0.881	0.702	Moderate descriptor coupling reflecting localized crater formation and flow divergence effects.
ARC 309	0.988	0.977	0.981	0.969	0.978	0.974	Exceptionally consistent correlations, confirming balanced erosion dynamics and effective damping of extreme asperities.

Overall, the heatmaps shown in Figure 9 clearly illustrate these relationships. The red cluster in the top left, representing the R_a–R_q–R_z group, signifies closely related descriptors primarily influenced by mean amplitude statistics. The apparent decline of the R_t diagonal in austenitic systems points to localized instability and crater saturation near the jet exit. Conversely, duplex welds display consistently strong correlation fields, suggesting uniform erosion kinetics and stable surface roughness development at different depths and process stages. These findings validate that R_a and R_q alone sufficiently represent surface integrity in duplex alloys, while a comprehensive evaluation of austenitic systems also requires R_t and R_z to accurately reflect depth-dependent surface irregularities.

3.6. Hydrodynamic Erosion Mechanism Interpretation

The earlier discussed trends in roughness can be explained by the fluid–particle dynamics in abrasive water-jet machining. Figure 10 shows a schematic of the jet–surface interaction, emphasizing three hydrodynamic regimes that change with depth: the core-flow zone, rebound zone, and energy-dissipation zone. These zones collectively determine how the surface morphology evolves as penetration progresses. The connection between jet-energy regimes and surface roughness is qualitatively summarized in Table 7, serving as a mechanistic link between jet physics and the surface texture parameters.

Figure 10a illustrates that right after jet impingement, the core-flow zone forms, maintaining high momentum in the abrasive stream and coherent particle trajectories. During this stage, most particle kinetic energy is preserved, and material removal mainly occurs through micro-cutting and slight shearing. According to Table 7, this hydrodynamic condition produces surface textures that are sharp yet uniform, characterized by positive or near-zero skewness ($R_{sk} > 0$) and consistent R_z/R_a ratios. Experiments show this behavior in the near-surface region (0.5–5 mm) across all weld systems, with TIG 309 and ARC 309 displaying particularly uniform erosion and height distributions close to Gaussian ($R_{ku} \approx 3$–4), reflecting controlled particle impacts and minimal turbulence.

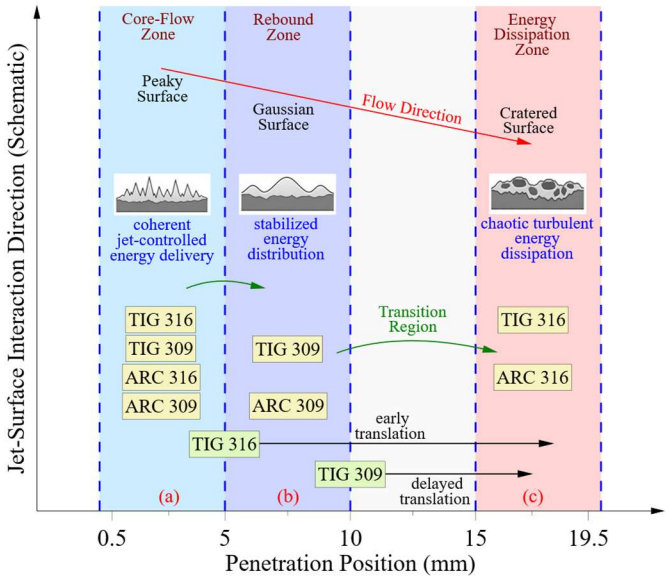


Figure 10. Schematic representation of particle-impact zones in AWJM: (**a**) core-flow region, (**b**) rebound zone, and (**c**) energy-dissipation zone. The arrow indicates the direction of abrasive water-jet flow and penetration.

Table 7. Qualitative mapping between abrasive water jet hydrodynamic energy regimes and surface roughness response across dissimilar welded systems.

Hydrodynamic Regime	Dominant Flow Characteristics	Typical Depth Range (mm)	Representative Parameters	Roughness Behavior	Weld Systems with Dominant Response
Core-flow zone	Coherent jet structure with high kinetic energy and shallow effective impact angle	0.5–5	$R_{sk} > 0$ $R_z/R_a \approx 5$–6	Peaky surface texture dominated by uniform micro-cutting and limited particle rebound	TIG 316 TIG 309 ARC 309 ARC 316
Rebound zone	Partially diffused jet with stabilized particle impact distribution and moderated momentum transfer	5–10	$R_{sk} \approx 0$ $R_z/R_a \approx 4$	Near-Gaussian surface profile with minimal roughness gradient and balanced peak–valley distribution	TIG 309, ARC 309 (dominant) TIG 316 (transitional)
Energy-dissipation zone	Turbulent kinetic-energy decay with particle rebound, scattering, and pressure pulsation	15–19.5	$R_{sk} < 0$ $R_{ku} \gg 3$	Cratered, valley-dominated surface with localized asperity collapse and roughness amplification	TIG 316, ARC 316 (dominant) TIG 309 (delayed/damped)

As penetration depth increases, the jet reaches the rebound zone, as shown in Figure 10b. In this area, some surrounding fluid is partially entrained, and abrasive trajectories slowly deflect, reducing the impact energy while impact angles become more perpendicular. This region is identified as the most hydrodynamically stable erosion regime, with the lowest roughness gradients and near-Gaussian surface textures ($R_{sk} \approx 0$, $R_z/R_a \approx 4$). Experiments indicate it occurs at depths of approximately 5–10 mm, notably in duplex welds (TIG 309 and ARC 309), which exhibit the most consistent correlation fields and minimal roughness variability. Austenitic welds (TIG 316 and ARC 316) only briefly enter this zone, reflecting a narrower window of hydrodynamic stability.

Beyond roughly 15 mm depth, the jet loses much of its momentum and moves into the energy-dissipation zone depicted in Figure 10c. In this area, erosion primarily results from particle collisions, pressure fluctuations, and chaotic rebounds, leading to random impacts and secondary crater creation. As shown in Table 7, this zone exhibits negative skewness ($R_{sk} < 0$), high kurtosis ($R_{ku} \gg 3$), and increasing extreme roughness measures (R_t and R_z), reflecting surfaces dominated by valleys and overlapping craters. This phenomenon is especially prominent in austenitic welds (TIG 316 and ARC 316), where the weaker relationship between R_t and R_z indicates a loss of jet coherence and unstable energy transfer. In contrast, duplex welds slow down and weaken this transition, maintaining more stable erosion due to their dual-phase microstructures.

In AWJM, erosion results from the interaction between jet coherence and the material's ability to dampen microstructural effects. When the jet stays coherent, surface formation occurs through stable micro-cutting, leading to uniform textures and low roughness variation. As coherence decreases with depth, jet momentum loss and particle rebound cause turbulent erosion and merging of craters, which increases roughness variability. Austenitic welds tend to become unstable at shallower depths due to their higher ductility and limited energy absorption, while duplex welds maintain stable erosion over larger depths because of their more balanced microstructural response. Therefore, Figure 10 and Table 7 together provide a comprehensive framework linking AWJM hydrodynamics, material behavior, and surface quality changes.

3.7. Optimization and Performance Window

The previous sections showed that surface quality in AWJM of different welded steels depends on three linked factors: (i) hydrodynamic energy delivery (water pressure and jet stability), (ii) exposure time (traverse speed and stand-off distance), and (iii) particle loading (abrasive flow rate). To develop a practical guideline, the roughness data was organized into a two-dimensional process-response map, displayed as a contour plot of R_a versus traverse speed and depth (Figure 11). This plot highlights the optimal zone, where jet energy, dwell time, and abrasive density come together to achieve the lowest average roughness, called the performance window.

Across all four welding systems, the contour distribution shows a typical pattern: a low-R_a "valley" at intermediate traverse speeds and depths of 5–10 mm, flanked by higher-R_a areas at both very low and very high traverse speeds. At lower speeds, extended impingement elevates the local energy density and causes crater overlap (as discussed in Sections 3.1 and 3.3), increasing R_a, especially in TIG 316 and ARC 316. Conversely, at higher speeds, the jet's footprint becomes narrower, reducing the energy per unit area. In the austenitic welds, this results in a resurgence of energy-decay roughness at 15–19.5 mm. The lowest R_a plateau occurs where the jet remains coherent but does not oversaturate the surface, correlating directly with the rebound/stable zone seen in the hydrodynamic schematic (Figure 10).

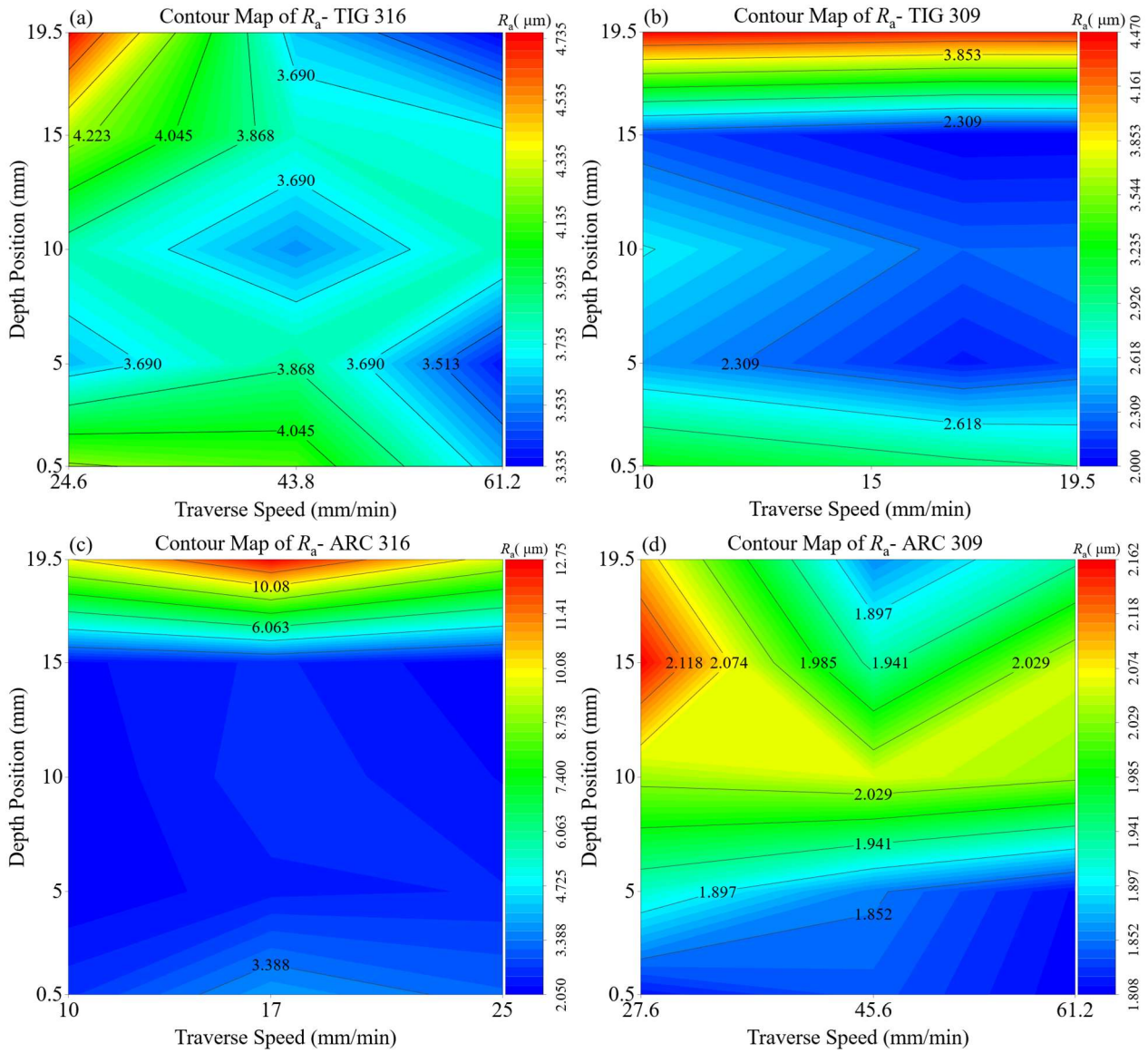


Figure 11. Contour maps of arithmetic mean surface roughness (R_a) as a function of traverse speed and depth position for dissimilar welded systems, highlighting the optimal low-roughness operating zone: (**a**) TIG 316, (**b**) TIG 309, (**c**) ARC 316, and (**d**) ARC 309.

Material behavior influences the width of this optimal range. Duplex welds (TIG 309, ARC 309) maintain a broad low-R_a zone because their microstructures distribute impact stresses evenly; they keep R_a at or below 2.5–2.8 μm across a wide speed range. Austenitic welds (TIG 316, ARC 316) reach similar R_a values only within a narrower speed window and are more affected by depth. This means their optimal range requires a slightly higher abrasive mass flow and, if needed, an intermediate stand-off distance of 4 mm to offset energy dispersion. These system-specific considerations are summarized in Table 8.

In summary, data from Figure 11 and Table 8 show that optimal AWJM performance depends on a balanced interplay of hydrodynamic energy density, exposure time, and abrasive concentration. When these factors are well-coordinated, the jet remains stable in the rebound zone, resulting in consistent erosion and Gaussian surface characteristics ($R_{sk} \approx 0$, $R_{ku} \approx 3$–4). However, if this balance is disturbed, due to too-long dwell times or loss of energy, the system becomes susceptible to excessive erosion and turbulence, as depicted in Figure 10.

Table 8. Optimal AWJM parameter summary (pressure, traverse speed, abrasive flow) per weld system.

Weld System	Water Pressure (bar)	Traverse Speed (mm·min^{-1})	SOD (mm)	Abrasive Mass Flow (g·min^{-1})	Depth Zone Giving Minimum R_a	Notes/Rationale
TIG 316	5500 (fixed)	43.8 (Level 2)	4 (instead of 3)	7	5–10 mm	Mid-speed reduces over-erosion; slightly higher SOD plus moderate AMF restores jet uniformity in austenitic weld.
TIG 309	4600–5000	17 (Level 2)	4	8	5–15 mm	Duplex steel shows widest stability band; $R_a \leq 2.6$ µm over mid-depth.
ARC 316	4600–5500	17 (Level 2)	4	8–9	5–10 mm	Needs more energy than TIG 309 due to coarse grains; AMF slightly higher to maintain cutting continuity.
ARC 309	5500 (fixed)	45.6 (Level 2)	3–4	7	5–15 mm	Most erosion-stable system; high pressure with mid-speed keeps $R_a \approx 2$ µm across depth.

This integrated optimization framework establishes a practical operating window: mid-range traverse speeds, moderate abrasive mass flow (7–8 g/min), and an intermediate stand-off distance (around 4 mm) produce the most stable surface response with $R_a \leq 3$ µm. These conditions align with the hydrodynamically stable rebound zone found in both duplex and austenitic welds, though the tolerances are narrower for the latter. The resulting process map acts as a predictive tool for selecting parameters, linking empirical roughness trends with physical jet-energy mechanisms. This understanding underpins the final conclusions, which organize the study's key correlations and optimization strategies into practical design recommendations.

4. Conclusions

This study systematically examined the surface integrity of four dissimilar stainless and carbon steel welds (TIG 316, TIG 309, ARC 316, and ARC 309) produced by abrasive water jet machining (AWJM). Using a comprehensive multi-parameter analysis that connected amplitude roughness metrics (R_a, R_q, R_t, R_z) with statistical shape factors (R_{sk}, R_{ku}) across different depth levels and traverse speeds, several key conclusions were drawn.

1. The depth-dependent roughness evolution identified three hydrodynamic regimes: the core-flow zone (0.5–5 mm), rebound zone (5–10 mm), and energy-dissipation zone (15–19.5 mm). Stable erosion and the lowest R_a values were observed in the rebound region, indicating that it is the primary window for surface formation.
2. The microstructure played a crucial role in the results. Duplex welds (TIG 309 and ARC 309) showed very consistent roughness measures (correlation coefficient $r > 0.95$) and textures close to Gaussian ($R_{sk} \approx 0$, $R_{ku} \approx 3$–4), suggesting even energy distribution and low turbulence. In contrast, austenitic welds (TIG 316 and ARC 316) showed signs of localized instability, such as deeper cratering and weaker correlation between R_t and R_z, which aligns with their higher ductility and reduced damping ability.
3. Statistical and mechanistic integration links correlation behavior (Figure 9) to hydrodynamic zones (Figure 10), showing that roughness uniformity is associated with peak jet coherence. The transition from stable rebound to dissipative turbulence is accompanied by the emergence of negative R_{sk} and higher R_{ku}, providing a quantitative measure of energy loss with depth.
4. Process optimization, shown in Figure 11 and summarized in Table 8, pinpointed the operational settings that reduce surface roughness: moderate system-specific traverse speeds (e.g., Level 2: 17–45 mm·min^{-1}), an intermediate stand-off distance (~4 mm), and a controlled abrasive flow rate (7–8 g·min^{-1}). These parameters keep R_a at or below 3 µm and produce statistically symmetric textures across weld systems.

5. The resulting performance map provides a predictive design framework that connects measurable process parameters with the underlying physics of jet energy. It enables the selection of AWJM settings tailored to the material microstructure, reducing the need for extensive experiments and improving reproducibility in hybrid weld systems.

In summary, this research links AWJM hydrodynamics, material behavior, and the development of surface roughness. It combines statistical texture measures with mechanistic jet models to establish a reliable process window for producing high-quality, low-roughness surfaces in stainless and carbon steel welds. These findings lay the groundwork for real-time process monitoring and future machine learning optimization of AWJM surface finishing.

Funding: This research received no external funding.

Institutional Review Board Statement: Not applicable.

Informed Consent Statement: Not applicable.

Data Availability Statement: The data presented in this study are available on request from the corresponding author due to privacy and legal reasons.

Acknowledgments: The author would like to express sincere gratitude to Umm Al-Qura University, Makkah, Kingdom of Saudi Arabia, for the valuable resources that facilitated this research.

Conflicts of Interest: The author declares no conflicts of interest.

Abbreviations and Symbols

The following abbreviations are used in this manuscript:

Symbol/Abbreviation	Description
AWJM	Abrasive Water Jet Machining
TIG	Tungsten Inert Gas welding
ARC	Manual Metal Arc welding
MMA	Manual Metal Arc welding
TIG 316	TIG-welded stainless–carbon steel joint using AISI 316 filler metal
TIG 309	TIG-welded stainless–carbon steel joint using AISI 309 filler metal
ARC 316	ARC-welded stainless–carbon steel joint using E316 electrode
ARC 309	ARC-welded stainless–carbon steel joint using E309 electrode
R_a	Arithmetic mean surface roughness
R_q	Root-mean-square surface roughness
R_t	Total height of the roughness profile
R_z	Ten-point mean surface roughness
R_{sk}	Skewness of the surface height distribution
R_{ku}	Kurtosis of the surface height distribution
P	Water-jet pressure
v	Traverse speed of the AWJM nozzle
SOD	Stand-off distance between nozzle and workpiece
AMF	Abrasive mass flow rate
r	Pearson correlation coefficient
$\Delta R_a/\Delta depth$	Gradient of arithmetic roughness along jet penetration depth
R_z/R_a	Normalized roughness ratio
ISO	International Organization for Standardization
SD	Standard deviation
RH	Relative humidity

References

1. Giudice, F.; Missori, S.; Scolaro, C.; Sili, A. A Review on Fusion Welding of Dissimilar Ferritic/Austenitic Steels: Processing and Weld Zone Metallurgy. *J. Manuf. Mater. Process.* **2024**, *8*, 96. [CrossRef]
2. Huang, C.-H.; Hou, C.-H.; Hsieh, T.-S.; Tsai, L.; Chiang, C.-C. Investigation of distinct welding parameters on mechanical and corrosion properties of dissimilar welded joints between stainless steel and low carbon steel. *Sci. Prog.* **2022**, *105*, 00368504221126795. [CrossRef] [PubMed]
3. Leong, K.H.; Johar, R.M.; Yeo, A.; Nor, M.N.M.; Jalil, M.N.A.; Khalid, A.N. Assessing the Effectiveness of Steel-Composite Hybrid Pipeline for Corrosive, High Pressure Applications. *Key Eng. Mater.* **2007**, *334*, 589–592. [CrossRef]
4. Iqbal, M.; Karuppanan, S.; Perumal, V.; Ovinis, M.; Rasul, A. Rehabilitation Techniques for Offshore Tubular Joints. *J. Mar. Sci. Eng.* **2023**, *11*, 461. [CrossRef]
5. Xue, H.; Wang, Z.; Wang, S.; He, J.; Yang, H. Characterization of Mechanical Heterogeneity in Dissimilar Metal Welded Joints. *Materials* **2021**, *14*, 4145. [CrossRef] [PubMed]
6. Sołtysiak, R. Analysis of structure and material properties in individual zones of welded joint. *J. Constr. Steel Res.* **2021**, *187*, 106978. [CrossRef]
7. Karkalos, N.E.; Karmiris-Obratański, P. A Comprehensive Study on the Challenges of Using Pure Water Jet as Post-Treatment of Abrasive Water Jet Milled Pockets in Titanium Alloy. *Appl. Sci.* **2024**, *14*, 1741. [CrossRef]
8. Hashish, M. Abrasive Waterjet Machining. *Materials* **2024**, *17*, 3273. [CrossRef] [PubMed]
9. Thakur, P.M.; Raut, D.N.; Lade, P.R.; Kudalkar, S. Development of operations in waterjet technology: A review. *Adv. Mater. Process. Technol.* **2024**, *10*, 3835–3884. [CrossRef]
10. Ceritbinmez, F.; Günen, A. Comparison of drilling of Inconel 625 by AWJM and WEDM. *Aircr. Eng. Aerosp. Technol.* **2024**, *96*, 329–336. [CrossRef]
11. Ng, P.S.; Srinivasu, D.S.; Babu, N.R. Modeling of abrasive waterjet generated kerf on the top layer of a multi-layered structure. *CIRP J. Manuf. Sci. Technol.* **2022**, *38*, 660–674. [CrossRef]
12. Manikandan, M.; Hemalatha, S.; Chandramauli, A.; Ambrose, S.; Alsalami, Z. Surface roughness analysis in AWJM for enhanced workpiece quality. *E3S Web Conf.* **2024**, *491*, 04019. [CrossRef]
13. Armağan, M.; Arıcı, A.A. Analysis based on surface and kerf performance in multi-simultaneous cutting of S235JR structural steel with abrasive water jet. *Mach. Sci. Technol.* **2024**, *28*, 415–437. [CrossRef]
14. Wu, F.; Flint, T.; Kindermann, R.M.; Roy, M.J.; Yang, L.; Robertson, S.; Zhou, Z.; Smith, M.; Shanthraj, P.; English, P.; et al. Evolution and formation of dissimilar metal interfaces in fusion welding. *Acta Mater.* **2023**, *258*, 119232. [CrossRef]
15. Dahmen, M.; Deniz, B.; Petring, D. Revisiting transport phenomena and their role in intermixing during dissimilar laser beam welding. *Procedia CIRP* **2020**, *94*, 726–730. [CrossRef]
16. Wang, H.; Guo, Y.; Wang, X.; Gao, H. On surface texture evolution in abrasive flow machining. *Mater. Manuf. Process.* **2024**, *39*, 1894–1909. [CrossRef]
17. Moghaddam, M.; Hajiyev, I.; Papini, M. Prediction and mechanism of surface evolution in high-pressure slurry jet micromachining of channels. *Precis. Eng.* **2023**, *82*, 251–269. [CrossRef]
18. Karkalos, N.E.; Thangaraj, M.; Karmiris-Obratański, P. Evaluation of the Feasibility of the Prediction of the Surface Morphologiesof AWJ-Milled Pockets by Statistical Methods Based on Multiple Roughness Indicators. *Surfaces* **2024**, *7*, 340–357. [CrossRef]
19. Pawlus, P.; Reizer, R.; Krolczyk, G.M. Modelling and prediction of surface textures after abrasive machining processes: A review. *Measurement* **2023**, *220*, 113337. [CrossRef]
20. Božić, D.; Trzun, Z.; Keran, Z. 3D roughness parameters in metal surface characterization. *Metalurgija* **2026**, *65*, 14–27. [CrossRef]
21. Alsoufi, M.S.; Bawazeer, S.A. Probabilistic Analysis of Surface Integrity in CNC Turning: Influence of Thermal Conductivity and Hardness on Roughness and Waviness Distributions. *Machines* **2025**, *13*, 385. [CrossRef]
22. Muralidharan, S.; Dinakar, N. A comparative investigation on weld metal properties of similar and dissimilar TIG welded joints on Al–Mg alloys. *Mater. Today Proc.* **2022**, *62*, 2217–2223. [CrossRef]
23. Oană, S.-A.; Karancsi, O.; Mitelea, I.; Uţu, I.-D.; Crăciunescu, C.M. The role of filler material selection in the laser welding process of deformable 6xxx series aluminum alloys. *Mater. Today Proc.* **2023**, *78*, 287–294. [CrossRef]
24. Afify, R.; Abdel-Aleem, H.; Gamil, M. Investigating TIG arc weldments for austenitic stainless steel 304 and 304L: A mechanical and metallurgical analysis. *Eng. Res. J. Shoubra* **2024**, *53*, 181–188. [CrossRef]
25. Bircan, M.; Pan, K.; Zhao, H.; Fan, J.; Dong, H. Microstructural Evolution and Mechanical Performance of A500 Bulletproof Steel Joints Welded with Austenitic and Ferritic Filler Materials. *Materials* **2025**, *18*, 929. [CrossRef] [PubMed]
26. Bobrovskij, I.; Zibrov, P.; Luk'yanov, A.; Levitskih, O. Integrated probabilistic surface roughness assessment for various processing methods. *EPJ Web Conf.* **2021**, *248*, 04007. [CrossRef]
27. Xie, J.; Rittel, D. Three-dimensional stochastic modeling of metallic surface roughness resulting from pure waterjet peening. *Int. J. Eng. Sci.* **2017**, *120*, 241–253. [CrossRef]

28. *ISO 17636-1*; Non-Destructive Testing of Welds—Radiographic Testing—Part 1: X- and Gamma-Ray Techniques with Film. International Organization for Standardization, ISO: Geneva, Switzerland, 2016.
29. *AWS A5.9/A5.9M*; Specification for Bare Stainless Steel Welding Electrodes and Rods. American Welding Society, AWS: Miami, FL, USA, 2013.
30. *AWS A5.4/A5.4M*; Specification for Stainless Steel Electrodes for Shielded Metal Arc Welding. American Welding Society, AWS: Miami, FL, USA, 2012.
31. Natarajan, Y.; Murugesan, P.K.; Mohan, M.; Khan, S.A.L.A. Abrasive waterjet machining process: A state-of-the-art review. *J. Manuf. Process.* **2020**, *49*, 271–322. [CrossRef]
32. *ISO 4288*; Geometrical Product Specifications (GPS)—Surface Texture: Profile Method—Rules and Procedures for the Assessment of Surface Texture. International Organization for Standardization, ISO: Geneva, Switzerland, 1996.
33. *ISO 16610-21*; Geometrical Product Specifications (GPS)—Filtration—Part 21: Linear Profile Filters: Gaussian Filters. International Organization for Standardization, ISO: Geneva, Switzerland, 2010.
34. *ISO 4287*; Geometrical Product Specifications (GPS)—Surface Texture: Profile Method—Terms, Definitions and Surface Texture Parameters. International Organization for Standardization, ISO: Geneva, Switzerland, 1997.

Disclaimer/Publisher's Note: The statements, opinions and data contained in all publications are solely those of the individual author(s) and contributor(s) and not of MDPI and/or the editor(s). MDPI and/or the editor(s) disclaim responsibility for any injury to people or property resulting from any ideas, methods, instructions or products referred to in the content.